The Meteoritical Society

Meteoritics & Planetary Science 43, Nr 1/2, 97–120 (2008)
Abstract available online at http://meteoritics.org

A TEM study of thermally modified comet 81P/Wild 2 dust particles by interactions with the aerogel matrix during the Stardust capture process

Hugues LEROUX[1*], Frans J. M. RIETMEIJER[2], Michael A. VELBEL[3], Adrian J. BREARLEY[2], Damien JACOB[1], Falko LANGENHORST[4], John C. BRIDGES[5], Thomas J. ZEGA[6], Rhonda M. STROUD[6], Patrick CORDIER[1], Ralph P. HARVEY[7], Martin LEE[8], Matthieu GOUNELLE[9], and Mike E. ZOLENSKY[10]

[1]Laboratoire de Structure et Propriétés de l'Etat Solide, UMR 8008, Université des Sciences et Technologies de Lille, F-59655 Villeneuve d'Ascq, France
[2]Department of Earth and Planetary Sciences, University of New Mexico, MSC 03-2040, Albuquerque, New Mexico 87131–0001, USA
[3]Department of Geological Sciences, 206 Natural Science Building, Michigan State University, East Lansing, Michigan 48824–1115, USA
[4]Institute of Geosciences, Friedrich-Schiller-University Jena, Burgweg 11, D-07749 Jena, Germany
[5]Space Research Centre, Department of Physics and Astronomy, University of Leicester, Leicester LE1 7RH, UK
[6]Materials Science and Technology Division, Code 6360, Naval Research Laboratory, 4555 Overlook Ave. SW, Washington, D.C. 20375, USA
[7]Department of Geological Sciences, Case Western Reserve University, Cleveland, Ohio 44106, USA
[8]Department of Geographical and Earth Sciences, University of Glasgow, Gregory Building, Lilybank Gardens, Glasgow G12 8QQ, UK
[9]Muséum National d'Histoire Naturelle, Laboratoire d'Etude de la Matière Extraterrestre, USM 0205 (LEME), Case Postale 52, 57, rue Cuvier, F-75005 Paris, France
[10]NASA Johnson Space Center, Houston, Texas 77058, USA
[*]Corresponding author. E-mail: Hugues.Leroux@univ-lille1.fr

(Submitted 22 February 2007; revision accepted 24 May 2007)

Abstract–We report the results of high-resolution, analytical and scanning transmission electron microscopy (STEM), including intensive element mapping, of severely thermally modified dust from comet 81P/Wild 2 caught in the silica aerogel capture cells of the Stardust mission. Thermal interactions during capture caused widespread melting of cometary silicates, Fe-Ni-S phases, and the aerogel. The characteristic assemblage of thermally modified material consists of a vesicular, silica-rich glass matrix with abundant Fe-Ni-S droplets, the latter of which exhibit a distinct core-mantle structure with a metallic Fe,Ni core and a iron-sulfide rim. Within the glassy matrix, the elemental distribution is highly heterogeneous. Localized amorphous "dust-rich" patches contain Mg, Al, and Ca in higher abundances and suggest incomplete mixing of silicate progenitors with molten aerogel. In some cases, the element distribution within these patches seems to depict the outlines of ghost mineral assemblages, allowing the reconstruction of the original mineralogy. A few crystalline silicates survived with alteration limited to the grain rims. The Fe- and CI-normalized bulk composition derived from several sections show CI-chondrite relative abundances for Mg, Al, S, Ca, Cr, Mn, Fe, and Ni. The data indicate a 5 to 15% admixture of fine-grained chondritic comet dust with the silica glass matrix. These strongly thermally modified samples could have originated from a fine-grained primitive material, loosely bound Wild 2 dust aggregates, which were heated and melted more efficiently than the relatively coarse-grained material of the crystalline particles found elsewhere in many of the same Stardust aerogel tracks (Zolensky et al. 2006).

INTRODUCTION

The Stardust mission objective was to collect samples from comet 81P/Wild 2 and deliver them safely to the curatorial facility at the NASA Johnson Space Center. The ejected comet dust was captured in low-density (0.01–0.05 g/cm^3) silica aerogel to minimize particle heating and other physical modifications that could occur during hypervelocity impact at 6.1 km s^{-1} (Tsou 1995). The tracks left by the impacting dust particles in the Stardust aerogel collectors are complex (Hörz et al. 2006). Most are bulb-shaped at the entrance hole with diameters progressively decreasing along the penetration length and with or without slender terminal portions, suggesting variations in the structure, mineralogy, and chemical composition of individual Wild 2 dust particles (Hörz et al. 2006). Most tracks contain particle fragments distributed along their walls. However, some particles penetrated deeply into the aerogel

matrix, and 10 μm wide grains of olivine, pyroxene, sulfides, and refractory Ca,Al,Ti-rich minerals were observed at the end of some tracks (Zolensky et al. 2006).

Aerogel, an underdense microporous medium, is composed of a rigid, three-dimensional network of nanometer-sized SiO_2 clusters linked together to form chains. The distance between chains, which defines the pore diameter, is typically 10 nm in size, resulting in a very high specific surface area, typically 1000 m^2/g. The thermal conductivity of aerogel is low, on the order of 0.02 W/mK. Theoretical models of the capture process showed that grains could survive hypervelocity penetration into aerogel, but thermal alteration could also occur (Anderson and Ahrens 1994; Trucano and Grady 1995; Anderson 1998; Dominguez et al. 2004). All of the incident kinetic energy of the projectile must be dissipated within a few millimeters and in a few microseconds. In the hypervelocity regime, a shock wave is generated in the track entrance area that causes deformation, heating, and evaporation of the aerogel along the trajectory of the incoming projectile, leaving a track that commonly has a surviving particle at the terminus (Anderson and Ahrens 1994; Dominguez et al. 2003). The low aerogel density results in a typical peak pressure of a few GPa for an impact at 6.1 km s^{-1} (Anderson 1998). The temperatures reached during impact are not easy to estimate because of the unusual compressibility of the target and the formation of a dense molten phase from the nanoporous network (Anderson 1998). At 6 km s^{-1}, temperatures could reach 10,000 K in the shocked aerogel at the track entrance (Anderson 1998) but peak temperatures in the impacting particle will be significantly lower. Along the particle trajectory, local heating could cause melting of aerogel yielding a dense SiO_2 glass. Heating will be confined to small volumes within the aerogel and it is probably heterogeneous due to the very low thermal conductivity of the aerogel (Anderson and Ahrens 1994; Anderson 1998; Dominguez et al. 2004).

Prior to the Stardust mission, the performance of the aerogel capture medium was tested by hypervelocity impact experiments using light-gas guns (Barrett et al. 1992; Hörz et al. 1998; Burchell et al. 1999; Burchell et al. 2006a) and in analog studies of debris material captured in low Earth orbit (e.g., Hörz et al. 2000). A variety of minerals survived in these experiments without significant melting, including delicate, large (100 microns in size) grains of minerals such as phyllosilicates and carbonates (Okudaira et al. 2004; Noguchi et al. 2007; Burchell et al. 2006b). Varying degrees of volatilization, melting, and ablation were demonstrated (Barrett et al. 1992; Okudaira et al. 2004; Noguchi et al. 2007). The recovered materials were frequently shattered, melted, and encased within the melted aerogel in which they stopped. These previous efforts clearly demonstrated the need to understand how the small and poorly cohesive, micro-porous aggregates of submicron grains anticipated among Wild 2 particles could survive hypervelocity capture.

The aim of this paper is to describe the interactions of Wild 2 particles with aerogel during hypervelocity impact capture by analytical transmission electron microscopy techniques of severely thermally modified grains in the Stardust aerogel collectors in order to understand the effects of the capture process. Questions we would like to address are: To what extent did Wild 2 materials mix with aerogel as a result of melting induced by hypervelocity impact? What is the spatial scale of mixing? Can we reconstruct the bulk composition and the original mineralogy of the incident particles? We will report here on the general petrological properties of submicron grains that were dispersed throughout silica aerogel. The data presented here were mostly obtained during the preliminary examination (PE) period of the Stardust mission. The results obtained by different investigators were discussed at a Stardust meeting (Pasadena, California, USA, November 3–5, 2006), and found to have excellent internal consistency, thus providing a comprehensive database for understanding the interactions between thermally processed aerogel and cometary particles.

SAMPLES AND ANALYTICAL PROCEDURE

Wild 2 dust was extracted from locations along tracks left in the aerogel. The samples were removed from aerogel at the NASA Johnson Space Center (JSC) Stardust curatorial facility. Details about extraction and manipulation can by found in Westphal et al. (2002) and Zolensky et al. (2006, supplemental online materials). The extracted particles and grains were embedded in EMBED-812 epoxy, sulfur, or WELD-ON 40 acrylic (for more details about embedding and ultramicrotomy procedures, see Matrajt and Brownlee 2006) for serial sectioning using an ultramicrotome. Electron-transparent sections (70–100 nm thick) were placed onto C-coated transmission electron microscope (TEM) grids and distributed to different laboratories.

The samples that we studied are summarized in Table 1. According to the Stardust nomenclature, the first prefix is the parent aerogel cell, for example, C2054. The second part of the sample name is the number of the separated aerogel piece that contains the captured particle. The third part of the sample number refers to the track number. The fourth number corresponds to a specific grain in the aerogel piece, and finally, the last number is the TEM grid number. For example, the sample C2044,2,41,2,1 is the TEM grid 1, made from grain 2, from track 41, which was located in aerogel piece 2 removed from aerogel cell C2044. The prefix "FC" refers to samples that were derived from a loose aerogel chip of unknown parentage in the comet collector. The samples for which we present results here originated from three tracks, numbered 35, 41, and 44. Eight samples have been studied from track 35 (Table 1). Figure 1 shows the location of the grains from which they have been prepared. Four samples from two different grains in track 41 were studied (Table 1).

Table 1. Allocated samples and institutions where the TEM studies have been conducted.

Track number	Allocation number	Institution[a] (analysts)
35	C2054,0,35,16,1	NRL (R. M. S. and T. J. Z.)
35	C2054,0,35,16,2	UNM (A. J. B.)
35	C2054,0,35,16,8	MSU (M. A. V. and R. P. H.)
35	C2054,0,35,24,1	UNM (F. J. M. R.)
35	C2054,0,35,24,7	MSU (J. C. B. and M. R. L.)
35	C2054,0,35,32,1	IG (F. L.)
35	C2054,1,35,44,6	UNM (F. J. M. R.)
35	C2054,0,35,51,3	LSPES (H. L., D. J., and P. C.)
41	C2044,2,41,2,1	IG (F. L.)
41	C2044,2,41,3,3	UNM (A. J. B.)
41	C2044,2,41,3,4	IG (F. L.)
41	C2044,2,41,3,6	LSPES (H. L., D. J., and P. C.)
44	C2004,1,44,4,2	LSPES (H. L., D. J., P. C., and M. G.)
44	C2004,1,44,4,3	UNM (F. J. M. R.)
?	FC3,0,2,1,6	UNM (F. J. M. R.)
?	FC3,0,2,1,1	NRL (T. J. Z. and R. M. S.)
?	FC3,0,2,2,1	LSPES (H. L., D. J., and P. C.)

[a]NRL = Naval Research Laboratory, Materials Science and Technology Division, Washington. UNM = University of New Mexico. MSU = Michigan State University. IG = Institute of Geosciences, University of Jena. LSPES = Laboratoire de Structure et Propriétés de l'Etat Solide, University of Lille.

One grain from Track 44 was studied in two adjacent samples (Table 1). Samples from unknown parentage include allocations FC3,0,2,1,1, FC3,0,2,1,6, and FC3,0,2,2,1. Each sample consisted of several TEM slices placed on a supporting thin film. Each TEM grid contained from 3 to 10 ultramicrotomed serial slices numbered consecutively.

The TEM results reported here were obtained at many institutions. At the University of Lille, we used a Philips CM30 (LaB6 filament, working at 300 keV) and a Tecnai G2-20 twin (LaB6 filament, 200 kV). Chemical compositions were measured using energy dispersive X-ray spectroscopy (EDS) with ThermoNoran and EDAX Si-detectors (CM30 and Tecnai, respectively). At the University of New Mexico, the analyses were performed using a JEOL JEM-2010 (200 kV) high-resolution TEM with point-to-point resolution of 0.19 nm, equipped with a LINK ISIS EDS system and a JEOL 2010F FASTEM TEM/STEM (200 kV) equipped with a GATAN GIF 2000 imaging filtering system and Oxford INCA/Isis EDS system. At Michigan State University, we used a JEOL 2200FS field-emission gun (FEG) TEM at 200 kV, with an Oxford EDS system. At Friedrich-Schiller-University of Jena, we used an energy-filtered 200 kV ZEISS LEO922 TEM with a ThermoNoran Six EDS system; and at the University of Bayreuth, selected analyses were taken using a Philips CM20 FEG STEM equipped with a Vantage ThermoNoran EDS system. At the Naval Research Laboratory, we used a JEOL2200FS TEM equipped with a Noran System Six EDS system and Gatan Ultrascan 1000 CCD. At the University of Glasgow, we used a FEI F20 field-emission nanoanalytical TEM equipped with an EDAX X-ray spectrometer and a Gatan ENFINA electron spectrometer. For additional information, see Zolensky et al. (2006, supplemental online material).

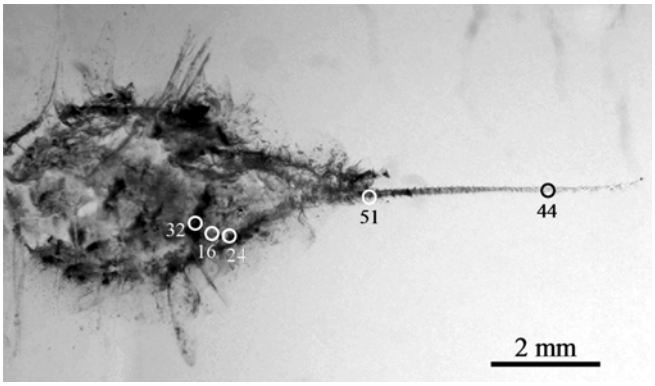

Fig. 1. Track 35 is 11.7 mm in length. The entrance area is bulbous and terminated by a long straight trail. The locations of the extracted grains for the present study are indicated by the open circles.

Most of us used standard techniques and procedures in data acquisition and thin film data reduction. Grain microstructures and compositions were studied using bright- and dark-field imaging in conventional TEM mode (parallel illumination), and also with annular-dark-field detectors in scanning (STEM) mode (convergent illumination). Crystallographic data were obtained by selected area electron diffraction (SAED). EDS detectors equipped with ultrathin windows were used for quantitative element analyses. We used probe sizes ranging from 5 to 15 nm, with either a fixed probe for spot analyses or a scanning probe for more spatially extended analyses. For quantitative analyses, calculations of element concentrations and atomic ratios were carried out using calibrated *k*-factors and thin film matrix correction procedures. The *k*-factors for the major elements were determined using standard minerals, according to the Cliff-Lorimer thin-film procedure (Cliff and Lorimer 1975) or by the parameterless method of Van Cappellen (1990). Some of us used *k*-factors provided by the EDS software manufacturers. For silicates, the absorption correction procedure based on the principle of electroneutrality has been applied (Van Cappellen and Doukhan 1994). For metal-sulfide assemblages, the TEM foil thickness was assumed to be the average thickness of ultramicrotomed sections (80 nm). Since EDS microanalysis is a relative concentration measurement, the total concentrations are derived by normalization to 100%. The relative errors are typically 2% for the major elements (O, Si, Mg, S, and Fe) and 20% for minor elements such as Cr and Mn. Element distributions were obtained by EDS X-ray intensity maps, using spectral imaging wherein each pixel of a spectrum image contains a full EDS spectrum. To display the distribution of elements, the intensity of characteristic X-ray peaks was integrated over a selected energy window corresponding to a peak of a given element. Upon image acquisition, it is then possible to quantify

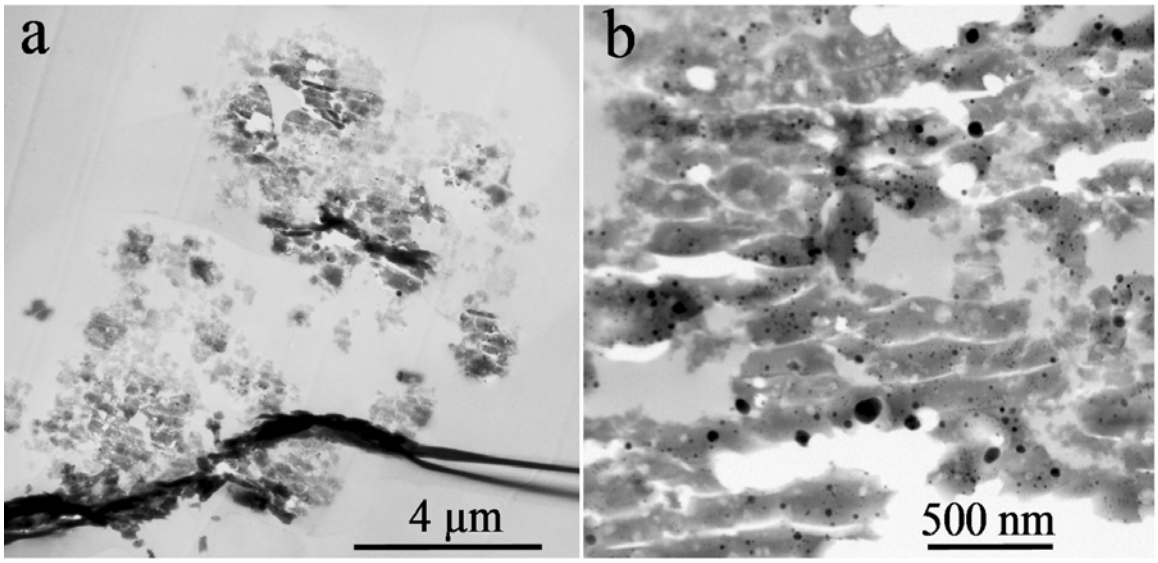

Fig. 2. a) Low-magnification bright-field TEM image showing an entire slice in C2054,0,35,51,3. The vitreous matrix (dark gray) appears discontinuous. The black curved linear features are due to sample preparation. b) STEM bright-field image showing the typical microstructure of the shard-like silica-rich glass matrix in the samples that contains variable but minor amounts of MgO, Al_2O_3, and/or CaO and has numerous opaque metal and sulfide inclusions dispersed in variable sizes and number distributions (sample C2004,1,44,4,2).

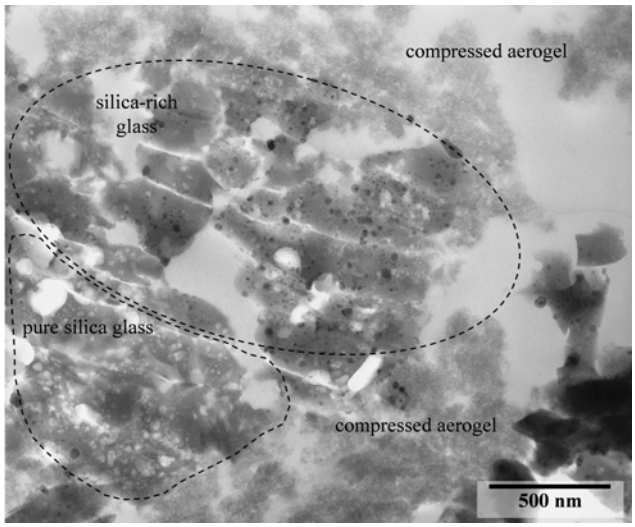

Fig. 3. Bright-field TEM image showing typical silica-rich glassy areas in contact with compressed aerogel, which is easily recognizable by its porous appearance, and a pure silica glass area containing numerous vesicles but no opaque inclusions (sample C2054,0,35,51,3). The irregular white areas are probably due to loss of sample material.

element concentrations of specific areas in each image by adding the corresponding spectra of adjacent pixels in order to get good counting statistics. Some representative areas were analyzed before the X-ray map acquisition and quantitatively processed in order to verify selected reference levels of element concentrations. Most EDS maps were recorded with a beam size of 5 to 10 nm with an intensity of 1000–2000 counts per second and a dwell time of 200 to 800 ms. The acquisition time ranged from 2 to 15 h. For the long duration experiments, we applied drift compensation and ensured a high vacuum to minimize contaminating the TEM slices.

RESULTS

General Description of the Samples

The most frequent and obvious microstructure is an extended, more or less continuous, shard-like vitreous matrix containing a large number of electron opaque inclusions and vesicles (Fig. 2). The shard-like aspect is due to ultramicrotomy sectioning, suggesting a brittle behavior of the samples. Local compositions range from pure silica to silica-rich, but some areas contain significant amounts of Mg, Al, Ca, S, and Fe. Opaque inclusions are typically Fe-Ni-S phases with variable Fe:Ni:S ratios.

In general, the pure SiO_2 glass contains numerous vesicles and is frequently found in contact with aerogel (Figs. 3 and 4). Aerogel is easily recognizable by the high number of nanopores, giving it a sponge-like microstructure (e.g., Stroud et al. 2004; Shi et al. 2006). Aerogel is present along the periphery of most of the samples where it was densified during the hypervelocity impact capture process. The aerogel in contact with the glassy matrix appears darker on the bright field TEM images with a mean pore size larger than pristine aerogel, suggesting that it was compacted. Dense silica glass and densified aerogel are both essentially pure silica but they are distinguishable by their relative X-ray Si and O count-rates during EDS microanalysis. Low-density aerogel generates a lower X-ray emission than the dense SiO_2 glass areas under the same EDS analytical conditions (see the Elemental Distribution in the Glassy Matrix section).

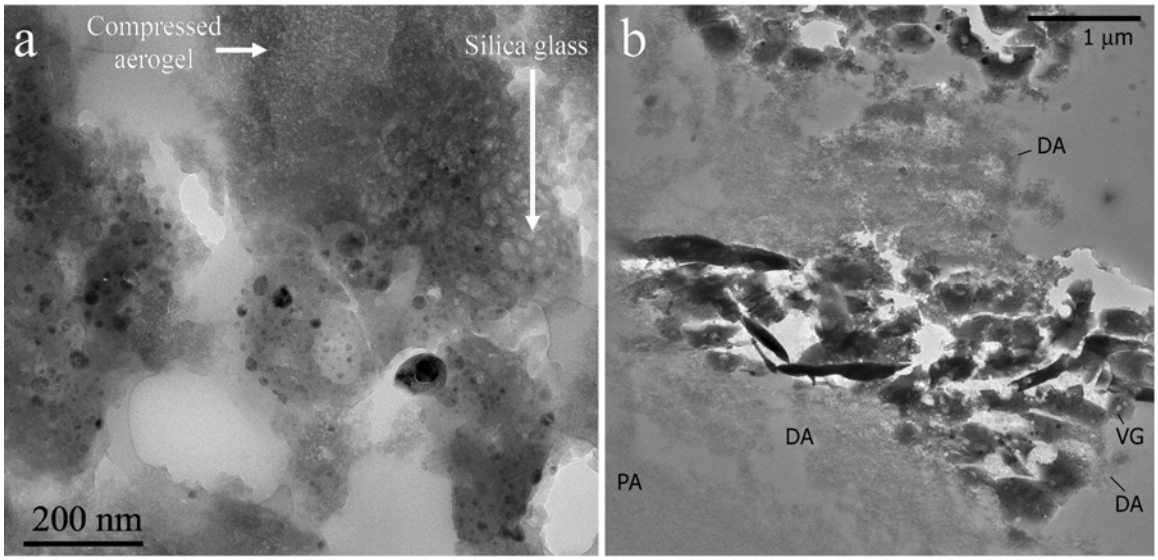

Fig. 4. Bright-field TEM images. a) Glassy matrix with high concentrations of opaque inclusions, compressed aerogel, and highly vesicular, pure silica glass (sample C044,2,41,3,4). b) Discontinuous glassy matrix in sample C2054,0,35,16,1, showing that the aerogel texture varies from fully pristine (PA) to densified (DA) to melted vesicular glass (VG). The uniform light to dark gray areas is the embedding medium used to prepare the ultra-thin sections. The irregular white areas are probably due to loss of sample material. The dark angular shards consist of glass.

The glassy matrix that contains Fe-Ni-S inclusions and vesicles (Figs. 2–4) is continuous in some TEM slices, but occurs as irregular small pockets in others. The silica-rich glassy matrix also contains Mg, Ca, Al, K, Mn, and Cr in variable concentrations. It occurs either free of opaque inclusions or with variable abundances of Fe-Ni-S inclusions. For glassy matrix without vesicles, the total number of cations other than Si can reach 15 at%. Frequently, the non-vesicular matrix does not contain opaque inclusions.

Bulk Composition of the Glassy Matrix

The EDS measurements of relatively large scanned areas of the glassy matrix in four different samples (FC3,0,2,2,1, C2004,1,44,4,2, C2054,0,35,51,3, and C044,2,41,3,6) show variable compositions (Table 2). In this table, areas of pure SiO_2 glass matrix have not been included. These compositions show that the material is overall silica-rich and heterogeneous with respect to the minor elements.

Since elements other than Si likely originate from the comet particles while Si is mainly due to the capture medium material, the degree of mixing can be represented by plotting the Si concentrations versus the sum of the concentrations of the other elements (Fig. 5). The data align on a simple mixing line whereby scattering around this line would represent deviation in composition from area to area of incident particle contribution, in particular to its respective metal + sulfide and silicate abundances. In order to give a comparison guideline, a few mixing proportions of a nominal CI material with pure silica are indicated (10, 20, and 30 at%). Most of the particle compositions are below 20% of a CI-like material.

The Fe/S ratio is highly variable from sample to sample. These variations are illustrated in Fig. 6, which plots the S and Fe concentrations normalized to Mg. Figure 6a has been constructed using analyses including both the glassy matrix and the Fe-Ni-S inclusions with large STEM scan areas. In this figure, we compare two samples (FC3,0,2,2,1 and C2004,1,44,4,2) that differ greatly. This difference could be due to various metal/sulfide proportions in the incident material or due to the presence of Fe in the silicates in the form of FeO. In Fig. 6b, we compare three samples (C2054, 0,35, 44,6, C2004,1,44,4,3, and FC3,0,2,1,6) with spot analyses taken in the silica-rich glassy matrix only, but which may contain small (<30 nm) Fe-Ni-S inclusions. These three samples also display strong differences in their S/Fe ratios and their Mg contents relative to Fe, but for each sample, the data points are considerably more scattered than in Fig. 6a for samples where the compositions were integrated over larger areas.

Finally, we have estimated the average composition of the samples. The results are shown in Table 3. In this table, the measured compositions are normalized to the total amount of elements, excluding Si and O and compared to their corresponding CI abundances. This table allows the first direct comparison of the bulk composition of an incident particle or fragment of a particle captured in these small silica glass volumes. The calculated average compositions are not far from the CI composition, but there are several significant deviations. For instance samples FC3,0,2,2,1, C2044,2,41,3,3, and C2054,0,35,16,8 are S-rich, suggesting that the particle precursors were sulfide-rich. In contrast, samples C2004,1,44,4,2 and C2004,1,44,4,3 are S-poor, suggesting that the sulfide component was not

Table 2. Representative EDS compositions (at%) for samples FC3,0,2,2,1, C2004,1,44,4,2, C2054,0,35,51,3, and C044,2,41,3,6. Relatively large areas of interest were randomly selected for scanning in the STEM mode. For each sample, the data were recorded with the same acquisition parameters (scanned surface, probe size, and probe intensity). They are long duration microanalyses, typically 200 s but up to 1000 s, with a count rate ranging from 1000 to 2000 cps/s.

O	Si	Mg	Fe	Ni	S	Al	Ca	Ti	Cr	Mn
FC3,0,2,2,1: scanned area = 300 × 300 nm; duration analysis = 200–500 s.										
64.5	31.6	0.87	1.52	0.07	1.29	nd	0.06	nd	nd	nd
65.4	32.3	0.62	0.85	0.07	0.71	nd	nd	nd	nd	0.02
65.2	31.8	1.07	0.83	0.03	0.72	0.29	nd	nd	0.02	0.02
63.4	30.0	2.80	1.6	0.05	1.7	0.32	0.07	nd	0.09	0.03
64.3	30.4	2.70	1.16	0.04	0.96	0.25	0.06	nd	0.03	0.05
C2004,1,44,4,2: scanned area = 2 × 1.5 μm; duration analysis = 300–1000 s.										
63.9	29.3	2.87	2.37	0.17	0.86	0.34	0.12	0.02	0.04	0.04
62.5	26.9	5.21	5.21	0.31	1.10	0.24	0.15	nd	0.03	0.05
64.0	29.2	2.24	2.24	0.16	0.64	0.27	0.14	nd	0.02	0.02
62.7	27.5	6.00	1.90	0.09	1.20	0.40	0.20	0.02	0.04	0.03
64.4	30.2	2.14	2.04	0.12	0.75	0.16	0.20	nd	0.03	0.02
C2054,0,35,51,3: scanned area = 200 × 200 nm; duration analysis = 300 s.										
64.9	30.9	1.92	1.42	0.06	0.59	nd	0.17	nd	nd	0.02
64.3	29.7	3.76	0.84	0.04	0.70	0.42	0.12	nd	0.03	0.03
65.2	31.9	0.88	0.99	0.03	0.78	nd	0.10	0.03	nd	0.03
65.9	32.0	1.41	0.43	0.10	0.15	nd	nd	nd	nd	nd
63.5	29.0	1.99	3.63	0.10	1.19	0.45	0.09	nd	0.02	nd
C044,2,41,3,6 3: scanned area = 200 × 200 nm; long duration analysis = 300 s.										
65.2	31.0	1.39	1.59	0.08	0.39	0.31	0.05	nd	nd	nd
65.5	31.8	0.80	0.95	0.08	0.54	0.32	nd	nd	nd	nd
65.1	30.1	3.32	0.64	0.02	0.16	0.58	0.03	0.03	0.04	0.02
65.1	30.4	1.52	1.51	0.09	0.38	0.95	nd	0.02	0.06	0.02
62.6	29.4	2.10	3.10	0.09	2.20	0.40	0.08	0.02	0.03	nd

nd = not detected.

present in high proportion in this fragment or that S-loss occurred during the hypervelocity impact process. These average compositions are rough estimates and probably reflect localized composition anomalies, as well as bias from the method used (spot or scanned-areas analyses). For instance, the two adjacent allocations C2004,1,44,4,2 and C2004,1,44,4,3 coming from the same parent grain display significant differences in their Mg and Al abundances, while the Fe and S are found quite comparable. The allocations C2044,2,41,3,3 and C2044,2,41,3,6 strongly differ in their Mg abundances although they come from the same parent grain from track 41. These differences are likely due local heterogeneities of the glassy matrix, which may have incorporated different incoming materials.

Metal/Sulfides Inclusions

The metal-sulfide inclusions have sizes ranging from a few nanometers to about one hundred nanometers in diameter. Their size distribution and density, i.e., the number of inclusions per surface unit at the microscale of opaque inclusions are variable among and within the samples (see, for instance, Figs. 2–4). All Fe-Ni-S inclusions have a sharp interface with the silica-rich matrix.

The Fe-Ni-S phases appear with two different textures: 1) inclusions with a mottled texture of a fine-scale polycrystalline intergrowth of two mineral species; this texture is common for the smallest spherical inclusions, and 2) inclusions with a mostly regular core-mantle texture (Fig. 7). The former are mixtures of kamacite and pyrrhotite, both confirmed by SAED. Occasionally the inclusions contain two sulfides or taenite. A typical core mantle grain has a metallic core and a sulfide shell. Figure 8 shows an EDS X-ray intensity map obtained for a large zoned inclusion and Fig. 9 shows energy filtered TEM images for such core-rim grain. Figure 10 shows a relatively large and rare core mantle inclusion with a dual metallic kamacite and taenite core and pyrrhotite rim. The largest inclusions are also predominantly spherical, but they are occasionally found to have more complicated shapes. These morphologies include:

1. A subhedral shell containing a spherical core (Fig. 10).
2. An elongated shell producing an ellipsoidal grain shape, although for some inclusions the sulfide rim can be highly irregular (Fig. 11a).
3. A euhedral or subhedral metallic core surrounded by a sulfide spherical shell.
4. A few inclusions that appear to be compound inclusions consisting of two discrete cores surrounded by continuous shell material, or a metallic dumbbell-shaped

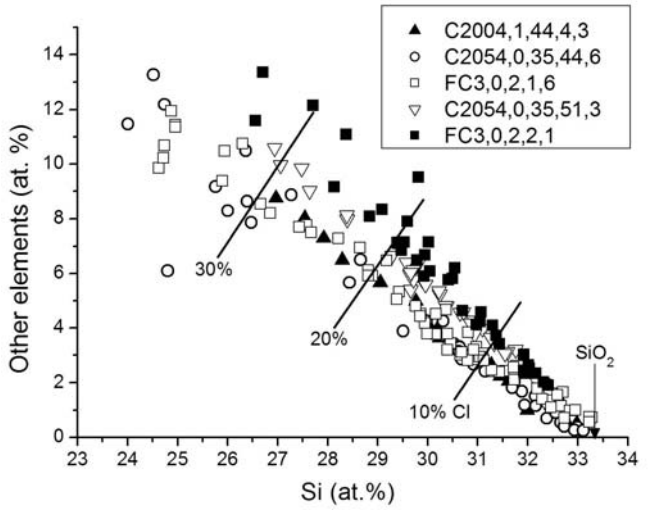

Fig. 5. Si (at%) as a function of the sum of all other elements (at%) for different randomly selected areas in samples FC3,0,2,2,1 and C2004,1,44,4,2 and random point analyses in the Si-rich glass matrix of C2054,1,35,44,6, C2004,1,44,4,3, and FC3,0,2,1,6. The data show a mixing line between the incident particles and the modified aerogel. For reference, we show the proportion of a nominal CI material admixed at 10, 20, and 30%. Pure SiO_2 is indicated at 33.3% Si (arrow).

core with sulfide "wings" (Fig. 11b), or even at the end of a thin sulfide tail (Fig. 11c).

5. A common non-spherical variant occurs at the interface between sulfide-decorated glass and empty volumes, as shown on Fig. 11d. In this variant, non-spherically symmetric inclusions are distributed at the interface, and are elongated with their long axes aligned along the interface.

The small (typically <40 nm) inclusions are most frequently spherical, i.e., dominated by surface tension (e.g., Fig. 7). Most of their bulk compositions are intermediate between iron mono-sulfide and pure Fe,Ni metal. The EDS composition measurement of individual phases is difficult because of their small size and the fact they are embedded in the 100 nm thick glass matrix foil. Thus the compositions may include some iron and sulfur present in the glassy matrix. The FeO content of the matrix is usually low (see the Elemental Distribution in the Glassy Matrix section) and the contribution to the total Fe of the inclusions will be negligible.

Compositions of large inclusions (>40 nm) can be measured individually without strong interference from the matrix. Ternary Fe-Ni-S representations are well suited to display the compositional variability. Figure 12a shows Fe-Ni-S ternary composition diagrams for four different samples for which the compositions were obtained from scanned areas that covered entire opaque inclusions, that is, they represent a bulk composition for each inclusion analyzed. The compositions lie along a mixing line joining the FeS composition with the metal Fe-Ni baseline,

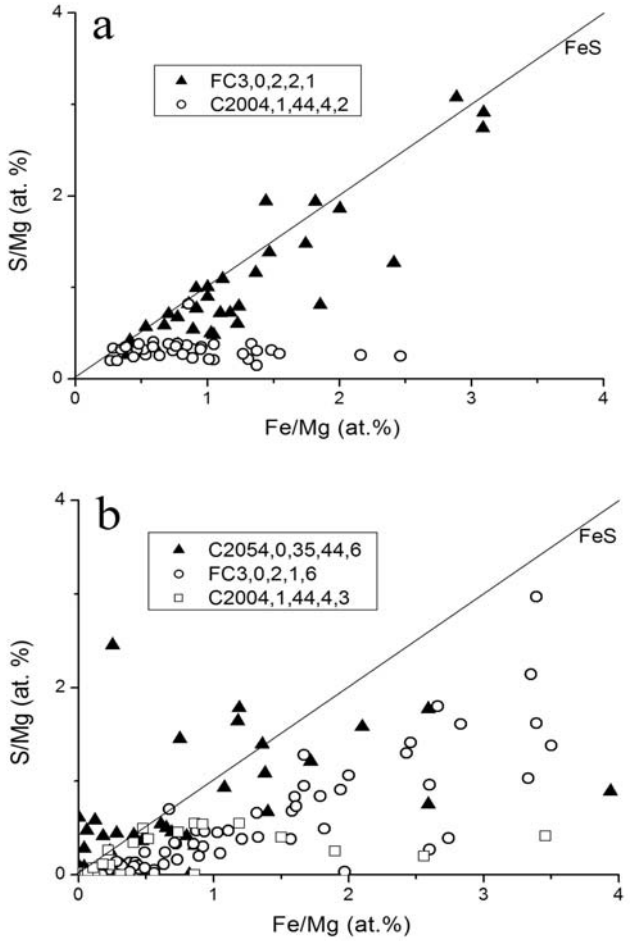

Fig. 6. S/Mg atomic ratio as a function of the Fe/Mg atomic ratio for (a) different areas in samples FC3,0,2,2,1 and C2004,1,44,4,2 recorded for relatively large scanned areas in the STEM mode, which include glassy matrix with opaque inclusions. The data for FC3,0,2,2,1 is close to the FeS line while S/Fe in sample C2004,1,44,4,2 is low, suggesting that metal dominates in opaque inclusions. b) Fe/Mg and S/Mg ratios for samples C2054,0,35,44,6, C2004,1,44,4,3. and FC3,0,2,1,6 obtained by spot analyses of the glassy matrix hosting the large Fe-Ni-S inclusions. Sample C2004,1,44,4,3 is Mg-rich relative to Fe and S; the data for C2054,0,35,44,6 and FC3,0,2,1,6 overlap but show little evidence for iron associated with FeS "high-sulfur" spots occur in C2054,0,35,44,6.

due to overlap of the 2 dominant phases in the inclusions (pyrrhotite and kamacite) during electron beam analysis. This mixing line will provide an estimate of the various proportions of metal and sulfide in the inclusions. Figure 12b shows Fe-Ni-S ternary diagrams constructed from spot analyses of inclusions >35 nm. Spot analysis allows the measurements of the rim composition without including the core component, as well as highlights the high compositional variability among the inclusions, causing the more pronounced scatter in these data compared to the data shown in Fig. 12a. For Figs. 12a and 12b, the compositions are mainly within a part of the ternary diagram

Table 3. Average compositions for 10 samples normalized to 100% were calculated without Si and O in order to reduce the contribution of aerogel for comparison with the CI abundances (CI are taken in Anders and Ebihara 1982). The extent of aerogel admixing with a nominal CI material is shown in the last column. The average compositions for samples FC3,0,2,2,1 and C2004,1,44,4,2 are for large randomly selected scanned areas in the STEM mode: 300 × 300 nm (FC3,0,2,2,1, 18 analyses) and 2 × 1.5 μm (C2004,1,44,4,2, 19 analyses). The average compositions for C2044,2,41,3,6 and C2054,0,35,51,3 mix individual analyses of large scanned areas and compositions extracted from EDS maps. The compositions have been averaged from 30–40 individual analyses. For FC3,0,2,1,6, the average composition was calculated using 73 random spot analyses (beam size = 15 nm) through the glassy matrix. The average abundances for C2054,0,35,44,6 are based on 48 point analyses in matrix material (beam size = 15 nm). Composition for C2004,1,44,4,3 were calculated from 19 random spot analyses (beam size = 15 nm) through the glassy matrix. The data for C2054,0,35,16,8 is an average of three different large scanned areas that each correspond to an entire ultrathin TEM slice or as much of it as could be imaged in low-magnification TEM mode. C2044,2,41,3,3 is the average of two separate slices of the same particle with large scanned areas covering the entire slices. Composition for C2054,0,35,16,2 is an individual analysis of an entire slice.

Sample no.	Mg	Al	Ca	Cr	Mn	Fe	S	Ni	Mg/Si	% CI
FC3,0,2,2,1	34	5.6	1.5	0.3	0.2	32	25	1.6	0.039	4
FC3,0,2,1,6	40	2.7	1.9	1.1	0.7	36	15	2.1	0.076	8
C2054,0,35,16,2	33	0.2	2.1	1.3	0.4	36	23	3.2	0.051	5
C2054,0,35,16,8	37	n.d.	2.8	1.1	n.d.	25	31	2.5	0.042	4
C2054,0,35,51,3	37	4.8	1.9	0.2	0.1	29	23	0.8	0.067	7
C2054,0,35,44,6	55	n.d.	0.9	0.2	0.5	21	21	1.0	0.071	7
C2044,2,41,3,3	20	n.d.	2.8	2.8	0.5	48	26	3.1	0.020	2
C2044,2,41,3,6	47	6.6	1.0	0.1	0.1	25	18	1.6	0.061	6
C2004,1,44,4,2	42	4.7	1.9	0.4	0.3	36	12	2.3	0.068	7
C2004,1,44,4,3	52	n.d.	Tr	1.2	Tr	36	10	0.3	0.080	8
CI	**38**	**3.2**	**2.1**	**0.5**	**0.3**	**32**	**18**	**1.7**		

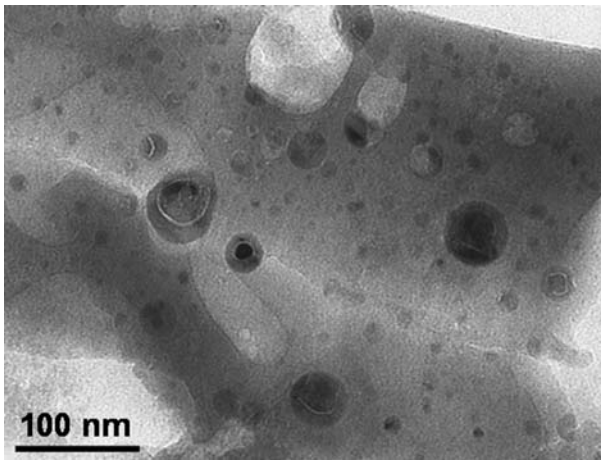

Fig. 7. Bright-field TEM image of several opaque inclusions with a metallic core and a sulfide mantle structure in the silica-matrix of C2054,0,35,51,3. Note the variable core/mantle ratios and the discontinuous core-mantle boundary in the largest inclusion, perhaps reflecting differential contraction during cooling. The ubiquitous, smaller inclusions are overwhelmingly homogenous grains. Several large vesicles (light gray) are present in the upper part of the image.

defines approximately delineated by the FeS and pyrrhotite sulfides, Fe metal, and metallic Fe,Ni with Ni/(Ni + Fe) of ~0.1, but with a preponderance of Ni-free and low-Ni compositions inclusions. Inclusions in C2054,0,35,44,6 and C2044,2,41,3,6 are dominated by iron sulfides, while inclusions in C2004,1,44,4,2 and C2204,1,44,4,3 are dominated by metallic Fe,Ni. In other samples (e.g., C2054,0,35,44,6), the S concentration in the rim can be well above the dominant iron mono-sulfide stoichiometry (50 at% and 53.3 at% for troilite and pyrrhotite, respectively), suggesting that sulfur or S-rich sulfides are present as a shell in some inclusions. The Ni concentrations can also be highly variable; in C2054,0,35,24,1 and C2054,0,35,24,7, they range from 5 to 75% in the metallic component. In sample C2054,0,35,51,3, we measured the inclusion compositions for two areas in the thin foil, each of them separated by several microns (Fig. 12c), which confirms a heterogeneous distribution of metal and sulfide on a micron scale. These diagrams indicate that the different areas contain different proportions of metal and sulfides. Altogether, these ternary Fe-Ni-S diagrams provide evidence for significant variability in the mineralogical properties and chemical compositions of opaque inclusions within and among samples. Table 4 summarizes the average composition of Fe-Ni-S inclusions in different samples and for six areas within C2054,0,35,51,3. In this table we have also calculated the average metal/sulfide molar ratios assuming all sulfides are close to the FeS stoichiometry as suggested by the FeS–metallic Fe-Ni mixing line. Table 4 also shows the calculated average Ni concentrations in the metal component, which ranges from 4.8 to 53.0 among all samples and from 4.8 to 14.0 within C2054,0,35,51,3, which is similar to the range for all samples when the data for C2054,0,35,24,1 would be a small-scale anomaly.

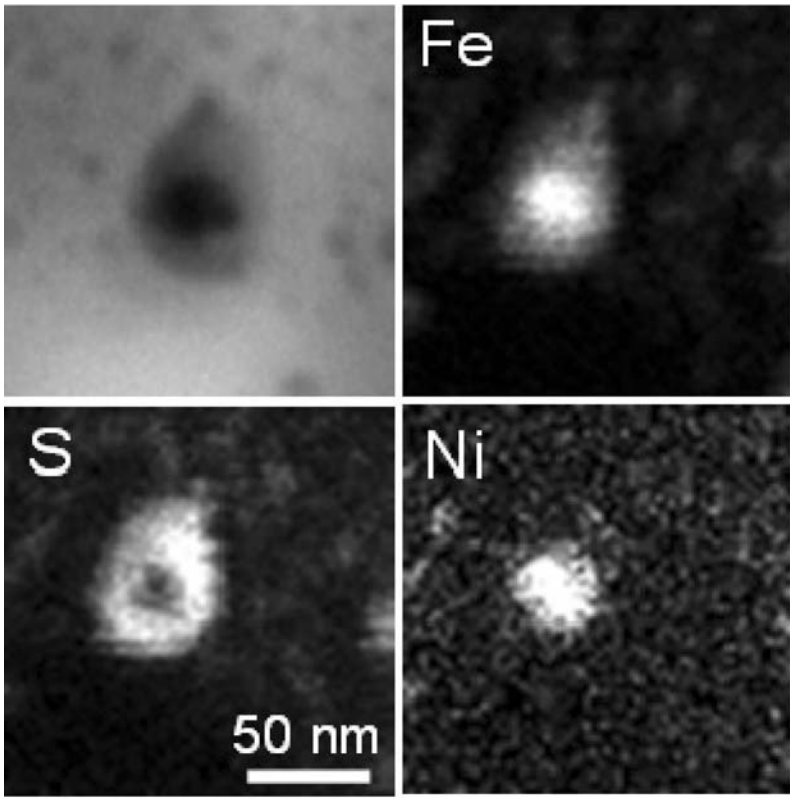

Fig. 8. EDS intensity distribution for Fe, S, and Ni of a large core/mantle inclusion in FC3,0,2,2,1. The metallic core that contains ~3 at% Ni is surrounded by an iron sulfide rim with a Fe:S ratio close to 1:1 at%.

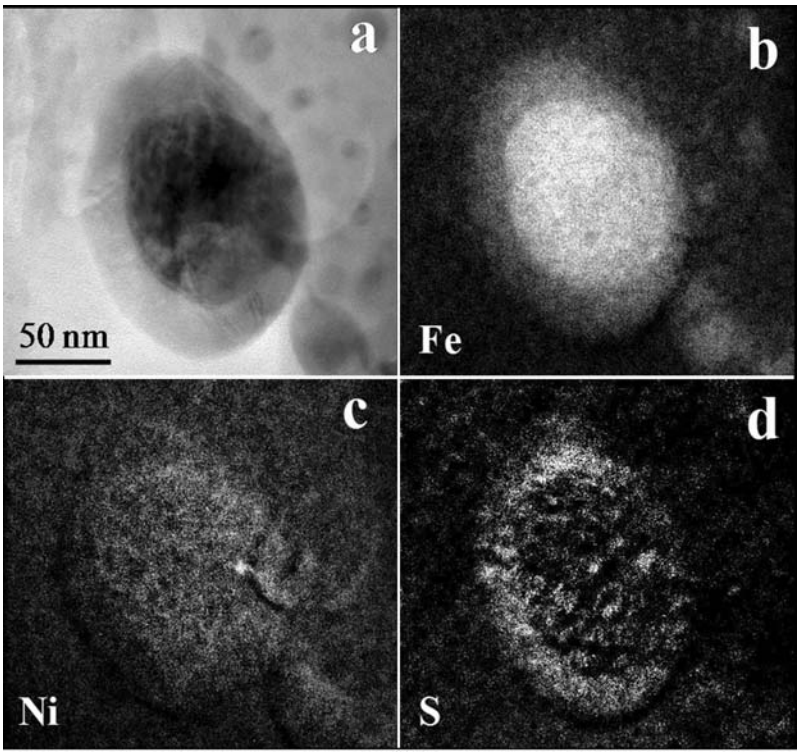

Fig. 9. Bright-field TEM and EFTEM images of composite metal-sulfide inclusions from C2054,0,35,16,2. a) Bright-field TEM image of a large metal-sulfide particle. b) Fe EFTEM map showing higher Fe content in the core of the particle. c) EFTEM Ni map showing this element resides predominantly in the core. d) EFTEM S map showing the rim of sulfide on the metal grain.

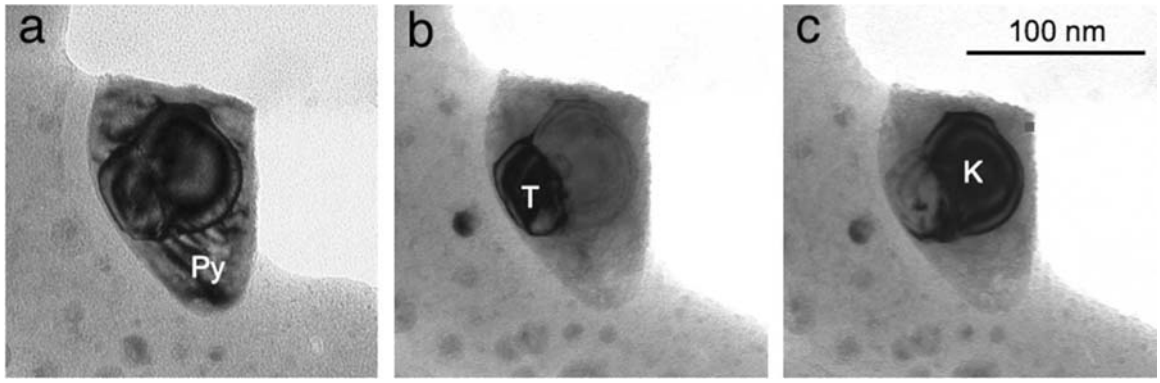

Fig. 10. a–c) Bright-field TEM images showing a large inclusion in C2054,0,35,51,3 that tends to have a subhedral shape. The inclusion is composed of a pyrrhotite rim (Py) and a duplex core of kamacite (K) containing 8 at% Ni and taenite (T) containing 19 at% Ni. These bright field images were taken with the grain in three different Bragg orientations. In (b) the taenite grain is under diffraction condition, while in (c) only the kamacite is diffracting.

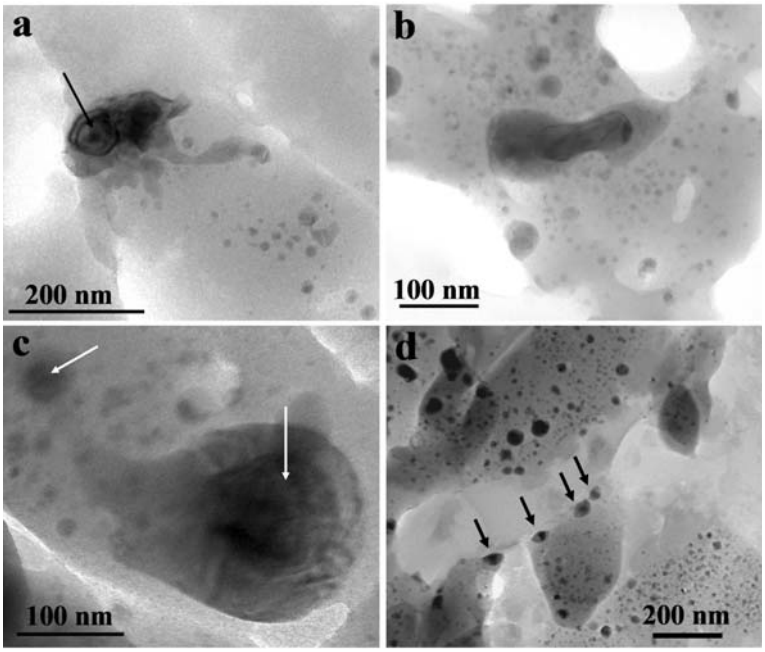

Fig. 11. a) Bright-field image showing an opaque inclusion in C2054,0,35,44,6 having an irregular shape with a long sulfide tail (Fe:Ni:S = 50:0.5:49.5 at%) with a distinct core (arrow), Fe:S = 85:15 at%. b) Dumbbell-shaped core (Fe:Ni:S = 86:2:12 at%; some S might be contributed by the sulfide rim along the e-beam path axis) with sulfide lobes (Fe:Ni:S = 50:1:49 at%). c) An extended compound inclusion with two discrete cores (arrows) joined by a sulfide tail in C2054,0,35,16,8. d) STEM bright field image showing non-spherically symmetric opaque inclusions with long axes aligned along free interface of silica-rich material in C2054,0,35,16,8 (see comment in text).

The sulfides in C2044,2,41,2,1, C2004,1,44,4,2 and C2044,2,41,3,4 may contain Cr in low concentrations (below 1 at%). In the metal fraction, P is also detected occasionally in concentrations up to 2.5 at% (C2044, 2,41,3,4). Although P is known to be a possible trace element in Fe,Ni metal, the relatively high amounts of P in a few Fe,Ni grains may be attributed to the presence of schreibersite in the precursor material. The sample C2004,1,44,4,3 contains ~100 nm size iron silicide, Fe_2Si to Fe_7Si_2, spheres that had formed during the impact when sulfide phases reacted with the silica capture media (Rietmeijer et al. 2008).

Elemental Distribution in the Glassy Matrix

The glassy matrix is dominated by silica (Fig. 5) but shows highly variable compositions on a submicron scale. Localized areas contain significant and also variable amounts of Mg, Ca, and Al as major elements. Table 2 shows representative analyses from four samples. Elemental distribution in the glassy matrix has been mostly studied using EDS intensity maps, providing valuable and informative element distribution images.

Figure 13 shows EDS X-ray intensity maps recorded in

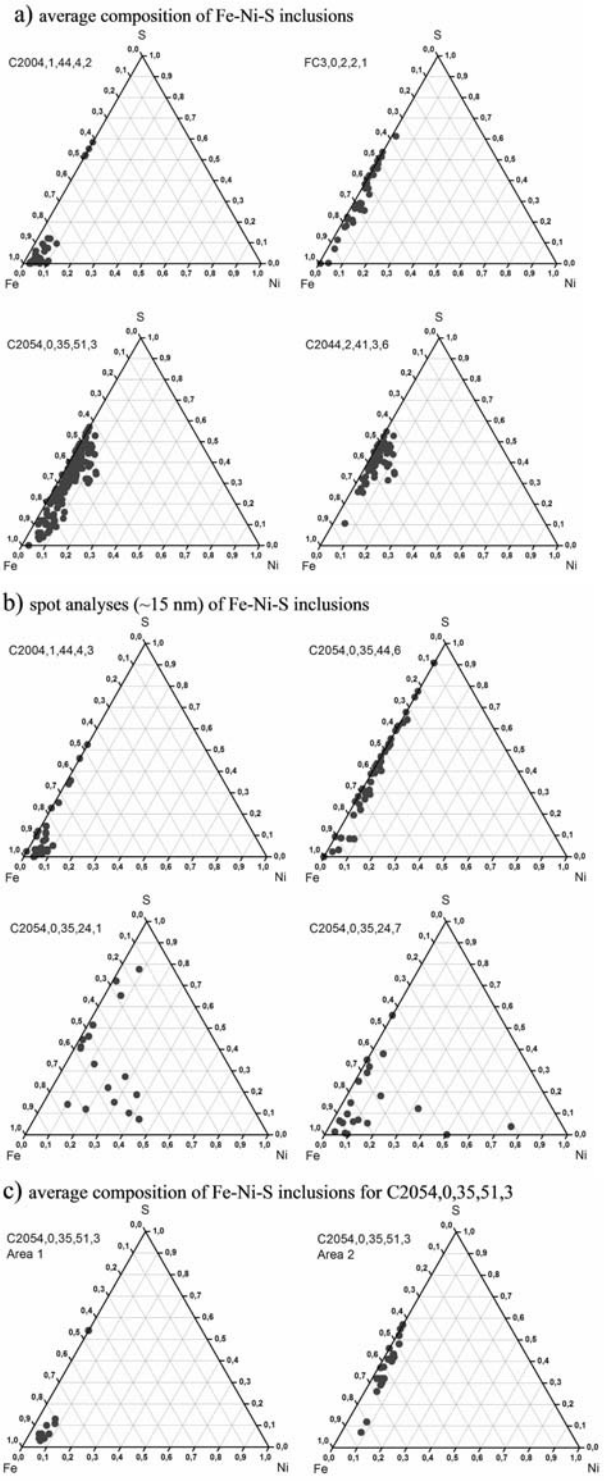

Fig. 12. a) Fe-Ni-S ternary composition diagrams (at%) for opaque inclusions in four samples based on scanning analyses of areas adapted to the sizes of the inclusions. Inclusions in C2004,1,44,4,2 are metal-rich. The compositions in C2054,0,35,51,3 and FC3,0,2,2,1 lie on a mixing line joining the FeS composition to the Fe-Ni baseline, suggesting variable proportions of metal and sulfides in the inclusions. C2044,2,41,3,6 is dominated by sulfide-rich inclusions. b) Fe-Ni-S ternary composition diagrams (at%) for opaque inclusions in four samples, based on spot analyses (15 nm). C2004,1,44,4,3 includes metallic grains; C2054,0,35,44,6 contains S-rich inclusions, suggesting that S-rich iron sulfide grains could be present. C054,0,35,24,1 and C054,0,35,24,7 contain Ni-rich phases. c) Fe-Ni-S ternary composition diagrams (at%) for two different areas in C2054,0,35,51,3. Area 1 contains predominantly low-S inclusions, while area 2 is sulfide-rich with compositions lying along a mixing line joining the FeS composition and the Fe-Ni baseline at Ni/(Ni + Fe) of ~0.1.

Table 4. Average compositions of Fe-Ni-S inclusions (at%).

Samples	Fe	Ni	S	N[a]	Metal[b] (mol%)	Sulfide[b] (mol%)	Ni(Fe)[c]
FC3,0,2,2,1	65.1	1.9	33.0	40	49	51	5.6
C2004,1,44,4,2	83.6	3.7	12.7	34	85	15	5.0
C2004,1,44,4,3	85.7	3.9	10.4	31	88	12	4.9
C2054,0,35,24,1	49.1	15.7	35.2	16	28	72	53.0
C2054,0,35,24,7	71.9	12.8	15.3	19	73	27	21.7
C2054,0,35,44,6	59.4	1.6	39.0	39	34	66	7.2
C2054,0,35,51,3[1]	60.8	4.2	35.0	22	42	58	14.0
C2054,0,35,51,3[2]	62.1	3.8	34.1	23	45	55	11.9
C2054,0,35,51,3[3]	83.7	5.4	10.9	11	87	13	6.9
C2054,0,35,51,3[4]	59.5	3.3	37.2	24	37	63	12.9
C2054,0,35,51,3[5]	77.2	2.9	19.9	18	74	26	4.8
C2054,0,35,51,3[6]	68.6	4.9	26.5	18	61	39	10.4
C2044,2,41,3,6	55.9	4.1	40.0	59	28	72	20.5

[a]N is the number of analyses used to calculate the average composition.

[b]The molar% of metal and sulfide is deduced from the average composition, assuming that the sulfides have FeS stoichiometry as suggested by a number of ternary diagrams.

[c]Ni concentrations in the metal phase assuming all Ni is partitioned in the metal phase only, as suggested by the chemical trends of opaque inclusions in Figs. 12a–c.

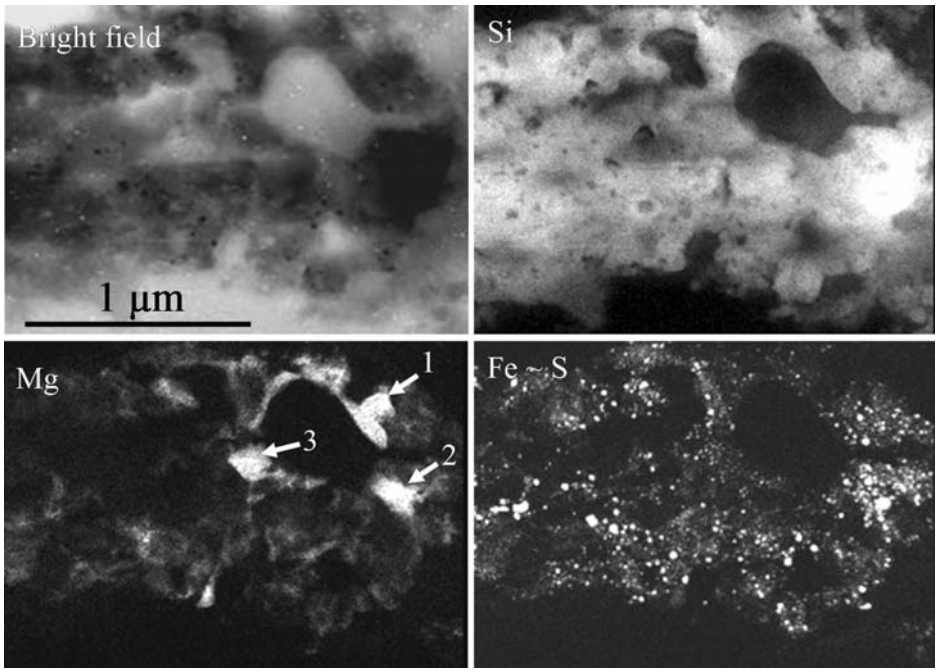

Fig. 13. Bright-field STEM image and EDS elemental distribution for Si, Mg, and Fe in the glassy matrix of FC3,0,2,2,1. The SiO_2-rich nature of the glassy matrix results in a good correlation between the Si map and the bright-field image. The distribution of Mg is strongly heterogeneous (arrows; the compositions for the Mg hot spots are given in Table 5). Note also the cloudy distribution of Mg in the Mg-poor areas. Iron is found mainly in the form of Fe-Ni-S inclusions.

FC3,0,2,2,1. The bulk composition of the area is high in silica (an average of ~95 at%). Thus, the Si distribution map shows a good correlation with the bright- and dark-field STEM images, with iron and sulfur found mainly in the opaque inclusions. In general, Fe, Ni, and S correlate well, showing that most inclusions contain these three elements. In most of the analyzed areas, magnesium forms a very low background with concentrations ranging from 1 at% to the detection limit estimated at 0.2 at%. Magnesium enrichment is found mainly as isolated patches (bright areas on the Mg intensity map), with a concentration within the range 5 to 7 at%, i.e., well below the magnesium concentrations in olivine or pyroxene. Compositions of these Mg-rich areas are given in Table 5.

Table 5. Representative compositions of "dust-rich" areas (at%). Most compositions were extracted from the EDS maps after acquisition by summing up the spectra of adjacent pixels, in order to gain counting statistics. Usually a few reference levels of element concentrations were recorded before the EDS map acquisition in order to verify the validity of compositions extraction from the maps.

	O	Si	Mg	Al	Ca	Cr	Mn	Fe	S	Ni
FC3,0,2,2,1: data extracted from the EDX map shown on Fig. 13.										
Area 1	64	29	5.2	0.47	0.04	0	0	0.59	0.61	0.04
Area 2	64	28	6.8	0.21	0.27	0	0.08	0.56	0.20	0.04
Area 3	64	29	5.4	0	0.22	0.05	0.03	0.78	0.27	0.07
FC3,0,2,2,1: data extracted from the EDX map shown on Fig. 14.										
Area 1	63	28	6.6	0.19	0.06	0.03	0.04	1.20	0.83	0.04
Area 2	64	28	7.1	0	0.11	0.04	0	0.79	0.43	0.02
Area 3	63	27	7.1	0.31	0.51	0.10	0	1.02	0.48	0
Area 4	64	28	0.8	4.5	0.13	0	0	0.49	0.98	0.08
C2044,2,41,3,6: data extracted from the EDX map shown on Fig. 15.										
Area 1	62	25	11.9	0	0.02	0.11	0.05	0.81	0.41	0
Area 2	62	24	13.3	0	0.10	0	0.04	0.87	0.21	0
Area 3	61	23	14.1	0	0	0	0.20	0.76	0.21	0
C2044,2,41,3,6: data extracted from the EDX map shown on Fig. 16.										
Area 1	61	23	13.5	1.23	0.33	0.09	0	0.47	0.24	0
Area 2	62	24	12.5	0.63	0.30	0.12	0.04	0.51	0.20	0.02
Area 3	62	23	13.0	0.77	0.32	0.16	0.03	0.48	0.20	0
Area 4	63	26	9.8	0.40	0.17	0	0.03	0.99	0.39	0
Area 5	62	25	10.9	0.42	0.11	0	0.04	1.08	0.50	0
Area 6	62	24	12.7	0.43	0	0	0.05	0.76	0.16	0.03
C2044,2,41,3,6: data extracted from an EDX map (not shown).										
Area 1	61	23	13.7	0.57	0.39	0.09	0.02	0.56	0.23	0
Area 2	61	22	14.6	0.48	0.43	0.19	0	0.57	0.19	0
Area 3	62	25	11.3	0.48	0.07	0	0.11	0.58	0.29	0
Area 4	62	24	13.0	0	0.12	0	0.04	0.93	0.33	0
C2054,0,35,51,3: data extracted from an EDX map (not shown).										
Area 1	61	24	11.6	0.33	0.37	0	0	0.9	0.9	0
Area 2	60	24	12.0	0	0.25	0	0.03	1.3	2.0	0.03
Area 3	61	26	8.7	0.3	0.28	0.03	0.03	2.0	1.9	0.03
Area 4	62	27	8.4	0.2	0.25	0.02	0.02	0.8	1.0	0.02
Area 5	62	25	9.8	0	0.77	0	0	1.2	0.9	0.03
Area 6	63	30	1.8	0	1.7	0	0.03	1.4	2.0	0.03
C2004,1,44,4,2: data extracted from an EDX map (not shown).										
Area 1	63	26	10.3	0.2	0.04	0.02	0	0.1	0.4	0
Area 2	62	25	11.0	0.3	0.07	0	0	1.5	1.4	0
Area 3	62	25	12.0	0.3	0.03	0	0	0.3	0.6	0
Area 4	62	26	9.0	0.4	0.31	0.04	0	0.8	0.8	0
C2054,1,35,44,6: glass areas without vesicles.										
Area 1	64	28	7.2	0	0.20	0.08	0.08	0.24	0.24	0
Area 2	62	25	10.9	0	0.25	0	0.12	0.20	0.51	0

Figure 14 shows another elemental distribution in FC3,0,2,2,1. In this area, the concentrations of Mg, Al, and Ca are heterogeneous. Four different patches can be distinguished. Areas 1 and 2 contain significant Mg but no Ca or Al. Area 3 contains Mg, which correlates with low concentrations of Ca, but Al is absent. Area 4 is strongly dominated by Al. Compositions of these four areas are given in Table 5. The boundaries of each area are relatively sharp and seem to delimit a ghost mineral assemblage.

Figure 15 presents an EDS intensity elemental distribution map recorded in C2044,2,41,3,6. This area includes two Mg-rich regions without vesicles and Fe-Ni-S inclusions, a SiO_2-rich area containing inclusions, pure SiO_2 vesicular glass, and compressed aerogel regions. In the Mg-rich regions, the compositions are relatively constant (Table 5), with a low concentration of Fe. Because these areas contain no inclusions, the ratio MgO/(MgO + FeO) can be estimated. This ratio is close to 97%.

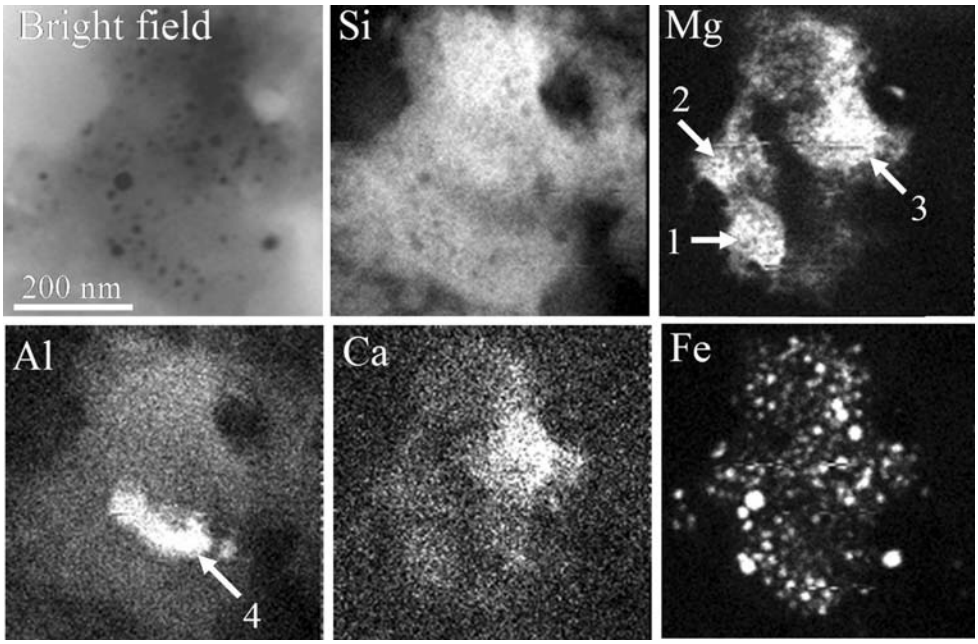

Fig. 14. Bright-field STEM image and EDS elemental distribution for Si, Mg, Al, Ca, and Fe in a glassy area of FC3,0,2,2,1. The region is composed of several subareas with different compositions that are listed in Table 5. Interfaces between the different zones are sharp suggesting they delimit a given compositional area. These possibly refractory grains could be an aggregate present in the comet.

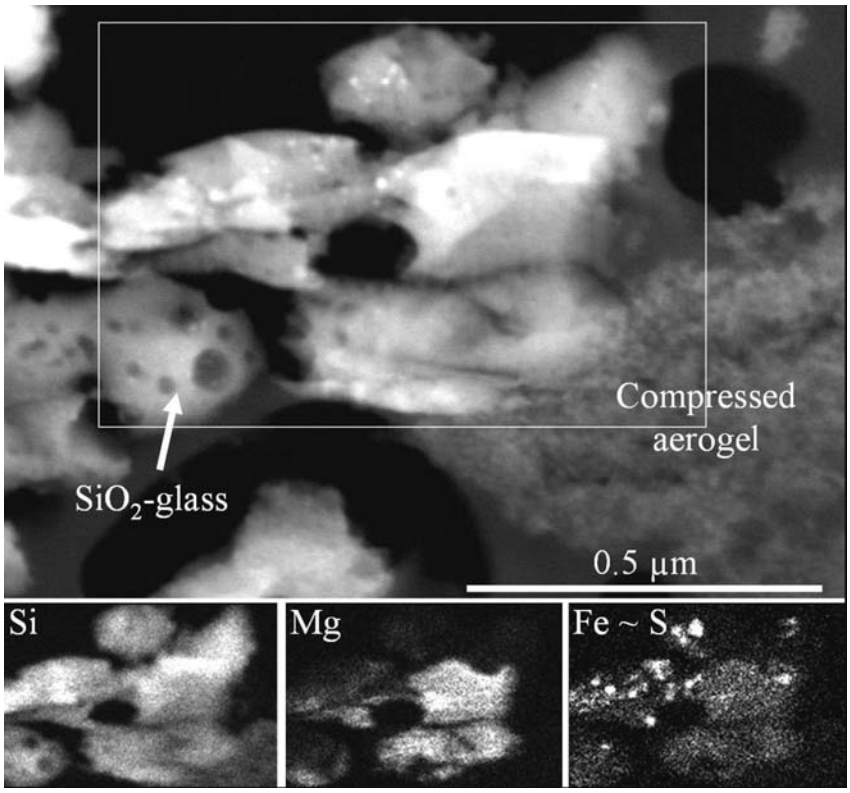

Fig. 15. Dark-field STEM image and EDS elemental distribution for Si, Mg and Fe in the silica-rich matrix with two Mg-rich domains of C2044,2,41,3,6 that also contain a highly vesicular almost pure silica glass domain. The Fe-Ni-S inclusions are absent in the Mg-rich areas, allowing the measurement of the amorphous domain MgO/(MgO + FeO) ratio (see Table 5). Note also the compressed aerogel zone at the lower right-hand corner. Its corresponding X-ray intensity is significantly lower than the dense silica area. The X-ray count rate in compressed aerogel is only 40% of those of dense silica glass, assuming a similar thickness for both materials. For an assumed density of ~2.2 g/cm^3 for the dense silica glass, the density for compressed aerogel is then calculated to be ~0.8 g/cm^3.

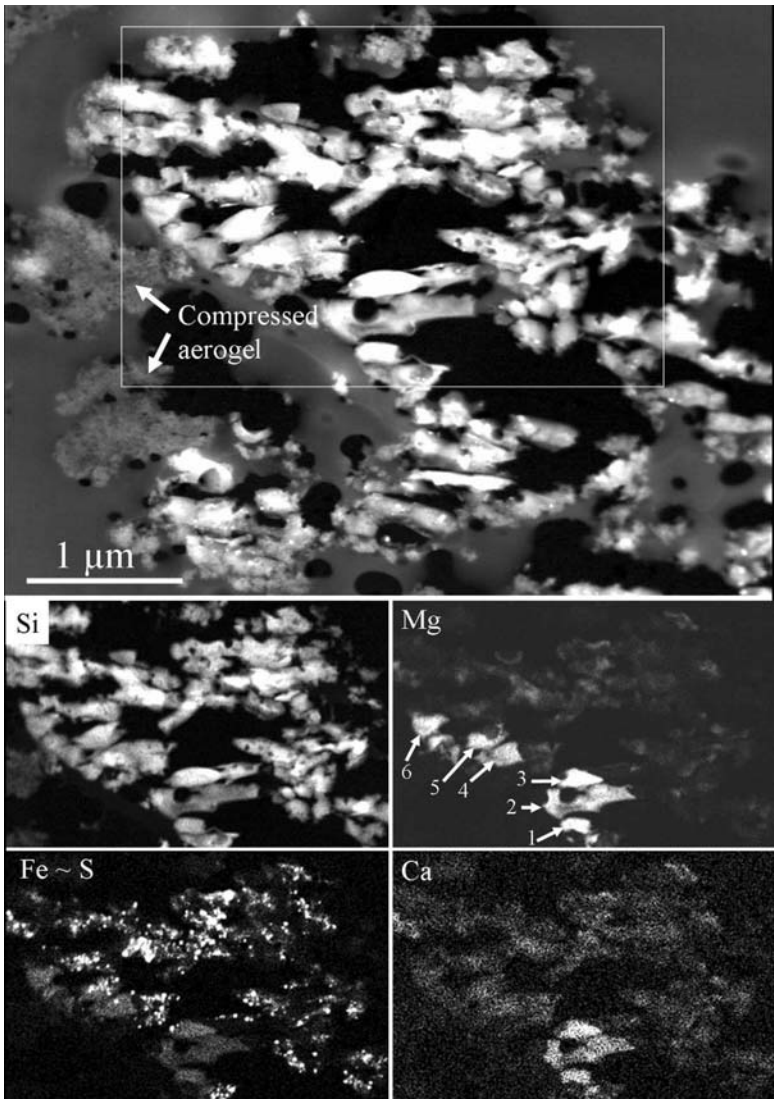

Fig. 16. Dark-field STEM image and EDS elemental distribution for Si, Mg, Fe and Ca in the silica-rich matrix, including vesicular domains of C2044,2,41,3,6. There are six Mg-rich shard-like domains that might represent two different grains that shattered during ultramicrotome section preparation. This type of shattering is a commonly observed experimental artifact associated with this sample preparation technique. One of these areas also contains Ca (arrow 1–3), while the other contains no Ca (arrows 4–6). Fe-Ni-S inclusions are not present in the Mg-rich and Ca,Mg-rich areas allowing the measurement of the MgO/(MgO + FeO) atomic ratio ~96%. Compositions of the six areas are shown in Table 5.

Figure 16 shows an EDS intensity map for C2044,2, 41,3,6. Two Mg-rich patches are present in this map. Areas 1–3 correlate well with Ca. The Fe-Ni-S inclusions do not overlap the Mg-rich regions and their MgO/(MgO + FeO) ratio is close to 97 at% for areas 1–3 and 4–6 (Table 5). In contrast to the glassy silica matrix, these Mg-rich areas do not contain vesicles.

Indigenous Grains in the Glassy Matrix

Indigenous crystalline silicates are rare in the glassy matrix. FC3,0,2,1,6 contains a polycrystalline Fe-rich olivine, $Fo_{78–82}$ grain (570 × 170 nm) (see Table 6 for the composition). This olivine was bordered on three sides by an amorphous silica-rich rim (90–120 nm wide) that contains no electron-opaque inclusions or vesicles, and a very sharp interface with the adjacent crystal. C2004,1,44,4,3 contains a regularly shaped, forsterite single-crystal (390 × 270 nm) (Fig. 17a; Table 6). A partial rim around the forsterite grain does not contain opaque inclusion, although the presence of a few nm-sized inclusions cannot be entirely excluded. The boundary between rim and crystal is razor-sharp. The compositions of the amorphous rim as a function of the distance from this interface relative to the typical silica glass matrix are shown in Table 6. The Mg content sharply decreases in the rim while the S and Fe

Table 6. Chemical compositions (at%) for crystals in sample FC3,0,2,1,6, C2004,1,44,4,3, and FC3,0,2,1,1. For FC3,0,2,1,6, the rim has been analyzed at ~50 nm from the interface. For C2004,1,44,4,3, the compositions of the amorphous rim were measured with increasing the distance of #1 to #3 from the olivine grain (see Fig. 17a). The estimated rim thickness is ~150 nm until its very sharp boundary with the glassy silica matrix with characteristic very small opaque inclusions. For FC3,0,2,1,1, the rim composition corresponds to the inclusion-free glass, in direct contact with pyroxene (see Fig. 17b). nd = not detected.

	O	Si	Mg	Al	Ca	Cr	Mn	Fe	S
Olivine and rim in FC3,0,2,1,6.									
Olivine	57.0	14.1	22.1	nd	nd	0.14	0.14	6.4	nd
Rim	62.7	24.4	7.0	2.1	0.13	0.04	0.11	3.4	nd
Olivine and rim in C2004,1,44,4,3; shown on Fig. 17a.									
Forsterite	56.9	13.8	28.7	na	nd	nd	nd	0.56	nd
Rim #1	62.2	24.9	12.1	na	nd	nd	nd	0.49	nd
Rim #2	62.7	25.4	10.4	na	0.33	0.20	nd	0.87	0.12
Rim #3	62.9	26.6	7.8	na	0.15	0.21	nd	1.4	0.86
Pyroxene and rim in FC3,0,2,1,1; shown on Fig. 17b.									
Pyroxene	60	19.4	18.8	0.6	0.5	0.2	0.2	0.4	nd
Rim	61.6	22.5	13.3	1.1	0.7	0.2	0.2	0.5	nd

contents increase, although no opaque inclusions were detected in the TEM images. Such inclusions would be small and deeply encased in the rim to escape TEM detection. In comparison, sample FC3,0,2,1,1 contains a subhedral pyroxene crystal (890 × 465 nm) (Fig. 17b). The grain is fractured along its lower-right edge and exhibits diffraction contrast on both sides of the fracture. The pyroxene appears to be encased in inclusion-free glass and surrounded by silica-rich, metal- and sulfide-bearing vesicular glass and aerogel. The glass in direct contact with pyroxene has a non-stoichiometric silicate mineral composition (Table 6). We interpret these olivine and pyroxene crystals as surviving, indigenous Wild 2 grains.

DISCUSSION

Stardust Wild 2 Dust Interactions with Aerogel

The Stardust mission's harvest included both intact, strongly physically (e.g., fragmentation) and thermally modified (i.e., a flash heating) cometary grains. The thermal modifications range from partial to complete melting and mixing with molten aerogel (Zolensky et al. 2006; Hörz et al. 2006). It is this last category of grains we studied. The main characteristic of our samples is the pervasive silica-rich glassy matrix, containing unambiguous compositional signatures of incident particles in the form of Fe-Ni-S inclusions and the presence of other elements such as Mg, Al, and Ca, among others, that were not part of the original aerogel. The resulting glass compositions are consistent with the admixture of incoming dust with a pure silica material resulting from melting and mixing of both components. Assuming a nominal CI composition for this Wild 2 dust, the observed glass compositions support up to 30 at% admixing with modified silica aerogel (Fig. 5).

The original silica aerogel consists of nano-clusters sticking to each other to form an low-density network. Cold compression of aerogel leads to densification due to the breaking and re-bonding of the ridges between clusters and interpenetration of clusters (e.g., Phalippou et al. 2004). The bulk porosity is reduced but not the specific surface area, and thus not the primary size scale of clusters and pores (Perin et al. 2003). The microstructure is not strongly modified since the material undergoes mainly brittle compaction. Thermal sintering is a way to produce dense glass from aerogel (e.g., Phalippou et al. 2004), but it is a kinetically dependant process. For instance, it requires several hours at 1050 °C to complete (Scherer et al. 1998; Perin et al. 2003). The melting temperature of aerogel corresponds to its glass transition temperature since aerogel is an amorphous material. For pure amorphous SiO_2, this transition occurs at ~1150 °C.

The returned Stardust aerogel materials contain both sponge-like and dense amorphous SiO_2 materials (Fig. 15) with different X-ray emission intensities. The EDS measurements performed on sponge-like microstructure suggest a density ~0.8 g/cm^3. It is much higher than initial aerogel density of 0.02 g/cm^3 and significantly lower than a normal SiO_2 glass (fused quartz, density ~2.2 g/cm^3). The spongy SiO_2 material is thus likely compressed aerogel, and the degree of compression is consistent with cold compression (e.g., Perin et al. 2003). In comparison, the dense SiO_2 material most likely formed through melting of aerogel rather than sintering because the kinetics of the latter process far exceeded the time it took to capture Wild 2 material. Thus, the co-existence of melted (glassy) and unmelted (spongy) aerogel indicates that strong thermal gradients existed at the submicron scale during Wild 2 dust capture. Evidence for melting is also given by the vesicular structure of the glassy matrix. The large vesicles might result from degassing of volatile molecules (e.g.,

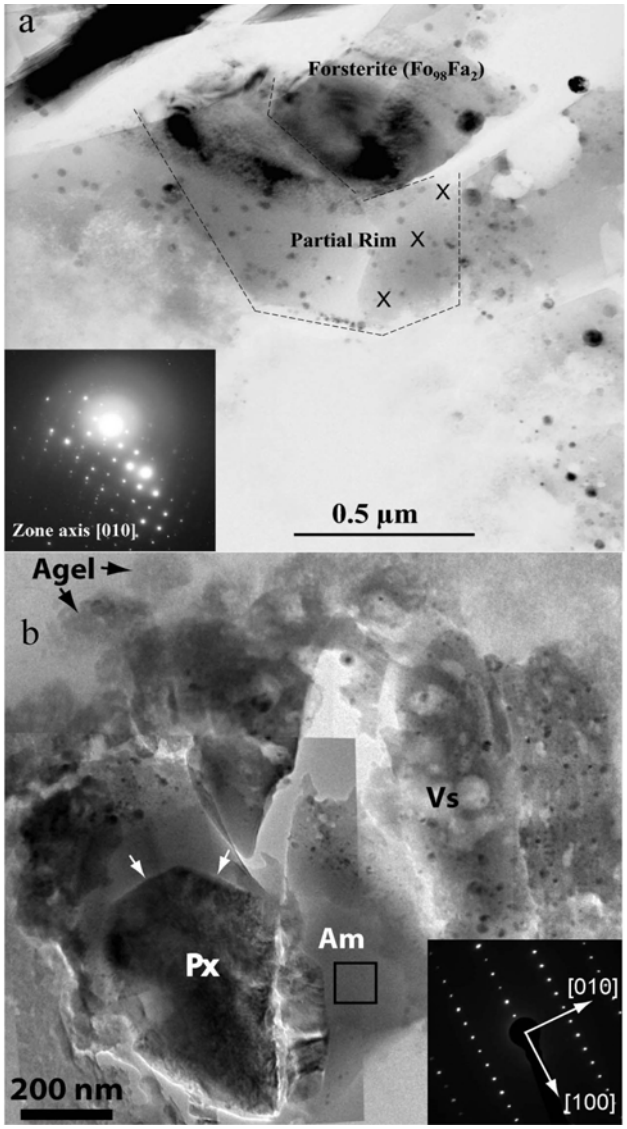

Fig. 17. a) Bright-field TEM image of a forsterite grain ($Fo_{98}Fa_2$) with its amorphous partial rim (dashed lines) in the silica-rich glass matrix of C2004,1,44,4,3. The inset shows the corresponding SAED pattern that 1) confirms its single-crystal nature and 2) the apparent lack of lattice deformation as indicated by the sharp, well-defined diffraction maxima. This image also highlights that, when conducting EDS analyses of objects in thin TEM slices of the silica-rich glass matrix, one has to be aware that the object of interest is not covered by a veil of matrix, as is the case in this particular image. Here the thin veil is recognizable by its tiny opaque Fe-Ni-S inclusions. Crosses indicate the location of the analyses shown in Table 6. The bright areas along the top of the image are an artifact of section preparation, but also show two large vesicles in the silica-rich matrix. b) Bright-field TEM image of a pyroxene grain (Px) with crystal facets (white arrows) that are associated with an amorphous material (Am) free of inclusions in FC3,0,2,1,1. The black rectangle indicates the location of the analysis shown in Table 6. Recognizable aerogel (Agel) is present at the top of the image. Highly vesicular silica-rich glass (Vs) with sulfide (arrowheads) and other opaque Fe-Ni-S inclusions appears on the right-hand side.

hydroxyl groups) on the surfaces or pores initially present in the original aerogel network.

Additional textural evidence indicates melting of Wild 2 material. For example, the compressed aerogel is found in contact with glassy areas either with or without sulfide inclusions containing major elements such as Mg, Al, Ca, Fe, Ni, and S that come unambiguously from the incident particles. The fine dispersion of Fe-Ni-S droplets within the silicate glass also strongly supports the high-temperature melting process. Indeed, most of the inclusions are spherical, i.e., dominated by surface tension. This microstructure is typical for molten Fe-Ni-S, with Fe-Ni-S droplets dispersed in a silica-rich melt. The EDS maps show that the impacting material is mainly present in the form of "dust-rich" patches distributed within the silica-rich glass. Most of these grains are amorphous suggesting that if they were originally crystalline, they were completely melted during the capture.

Fe-Ni-S Droplets

Silicate and Fe-Ni-S melts are immiscible. The spherical shape of metal and sulfide inclusions that is governed by surface tension of a liquid phase is typical for a rapidly quenched impact melt of these two immiscible molten components. Such morphologies occur in shocked chondrites (e.g., Bennett and McSween 1996; Leroux et al. 2000) and in micro-craters from solar cells returned from low Earth orbit (Kearsley et al. 2007). The fine-scale and ubiquitous dispersion of droplets within the silicate melt is due to the low viscosity of the metal-sulfide melt that was injected by the hypervelocity impact into the aerogel capture cell. During the high-temperature stage, coalescence of droplets probably did not occur to any significant degree, as we observed innumerable tiny droplets. It also suggests a high cooling rate after the peak thermal pulse. The spherical shape of the droplets indicates that their solidification was not accompanied by flow of the silica-rich matrix, suggesting that the solidification of the glassy matrix mainly occurred under static conditions. In some rare circumstances, droplets were still moving through the silica matrix while forming and cooling, as shown by the grain with elongated sulfide rim (Fig. 11c) and the grain with the irregular tail (Fig 11a). The dumbbell grain (Fig. 11b) suggests coalescence of two droplets, but the new forming droplet did not acquire the final, equilibrated, spherical shape. These are three observations with potential information on the thermal history of largest Fe-Ni-S inclusions with their characteristic core-mantle texture that could be different from the smaller opaque inclusions.

The crystallization sequence in the droplets can be deduced from the Fe-Ni-S phase diagram (Kullerud et al. 1969; Hsieh et al. 1982, 1987), the Fe-S binary phase diagram (Kullerud et al. 1969), or the modified binary Fe-S diagram (Rietmeijer et al. 2008). According to these phase diagrams, the crystallization temperature and crystallization sequences are a function of the (Fe + Ni)/S ratio of the melt. Metal Fe,Ni crystallizes first in the Fe-rich droplets, while iron sulfide will form prior to metal in the S-rich droplets. Crystallization in both cases ends at the eutectic temperature of ~1000 °C. With regard to the metal inclusions present in the silica matrix we note that the co-existence of kamacite and taenite in quenched impact melts was observed in the Tenham L6 chondrite (see Leroux et al. 2000). The core-mantle structure of the solidified droplets might be due to differential interfacial energies for the metal/silicate and sulfide/silicate interfaces. Thus the centers of the droplets are composed of Fe,Ni metal while the sulfide fraction is located at the rims of the droplets. Note that pentlandite has not been observed in these impact melts. Pentlandite formation from a melt is not obvious. It can be formed by a peritectic reaction (Sugaki and Kitakaze 1998) or from a further solid phase reaction (Kullerud et al. 1969). Both mechanisms are unlikely since they require solid state diffusion that cannot occur significantly because of the high cooling rate.

The opaque inclusions are dominated by kamacite and pyrrhotite. The high dispersion of data along the join between FeS composition and the Fe,Ni baseline illustrates that the metal-sulfide proportions are highly variable between droplets. In Table 4 we have summarized our EDS measurements on the Fe-Ni-S droplets. The data support several trends:

1. Some samples appear relatively homogeneous. This is the case for grain 4 in track 44, which has been studied independently (C2004,1,44,4,2 and C2004,1,44,4,3, which correspond to adjacent microtomed slices). Their ternary Fe-Ni-S composition diagrams are very similar (Figs. 12a and 12b), as well as their average composition (Table 4). The droplets are strongly dominated by kamacite, with a Ni concentration of 5 at%.
2. In contrast, C2054,0,35,51,3 appears highly heterogeneous (Fig. 12c; Table 4). The metal/sulfide molar ratio is highly variable, from 37/63 to 87/13. This situation probably reflects incorporation of different amounts of sulfide and metal precursors at different locations in the melt.
3. Several grains extracted from track 35 were studied (grains 16, 24, 32, 44, 51; see Fig. 1). The average compositions of the metal-sulfide droplets differ significantly from sample to sample. The molar metal/sulfide ratio ranges widely from 28/72 to 87/13. The metal phase is also highly variable in its composition. For instance, C2054,0, 35,24,1 is Ni-rich, suggesting the presence of taenite in the incident particle. The compositional variations suggest that a) different fragments of incoming dust were different in their initial metal/sulfide modal abundance and composition despite the fact that they come from the same parent track, thus from the same incident particle, or b) the maximum melting temperatures and/or cooling rates were different on small scale in this track.
4. The ternary diagrams (Fig. 12b) show a few high sulfur points. The nature of these particular compositions is uncertain with regard to the question whether they are FeS_2 (pyrite) minerals or thermally-evolved, heated Fe-S phases such as those found in flash-heated sulfide interplanetary dust particles (IDPs) (Rietmeijer 2004).

From synchrotron X-ray fluorescence studies, Flynn et al. (2006) have deduced that S loss could have occurred during Wild 2 grain capture. In the samples we have studied, the metal/sulfide molar proportions range from 88/12 in C2004,1,44,4,3 to 28/72 in C2044,2,41,3,6 (Table 4). In several samples, the molar ratio is close to 80/20 and 60/40 for H and L chondrites, respectively (averages calculated from Jarosewich 1990). Thus, the sulfide component in the collected Wild 2 dust does not appear to be depleted when compared to the bulk H and L chondritic abundances. Only two samples are S-poor (C2004,1,44,4,2 and C2004,1,44,4,3; both originated from the same parent grain). Unmelted terminal particles have been demonstrated to include both Fe,Ni metal, iron sulfides, and pentlandite (Zolensky et al. 2006). These phases were probably also

present among the fine-grained portion of original loosely aggregated Wild 2 dust, and are thus similar to aggregate and cluster IDPs in which silicate and sulfide minerals occur in distinct size fractions (Rietmeijer 1998, 2002). The relative proportion of each phase has not yet been determined in the Stardust samples. Melting and mixing of the components can account for the metal and sulfides droplets we have observed. The high metal fraction of some samples could be due to volatilization of S, but the extent of S loss cannot be determined from our observations without knowing the nature of the initial precursors.

Silica-Rich Glassy Matrix

The studied samples consist of silica-rich glassy materials suggesting that the original comet materials were almost fully melted and mixed to some extent with molten aerogel with variable degrees of intensity. Only rare submicron crystalline olivine and pyroxene grains survived intact (cf. the Indigenous Grains in the Glassy Matrix section). The peak temperature during particle penetration into aerogel reached values higher than the melting temperatures of refractory components such as olivine and pyroxene. At these temperatures, aerogel, Fe,Ni metal, and sulfides are also fully melted. The calculated amount of Wild 2 dust mixed in the glassy matrix is typically ~10 at%, assuming that the original dust had a CI composition. The melted incoming dust particles were thus mixed with a large portion of melted aerogel.

The Wild 2 dust component is not distributed homogeneously in the melted aerogel, as illustrated by the Mg-Ca-Al-rich patches (Figs. 13–16). Despite a significant concentration of elements, which originated from Wild 2 silicate materials, these dust-rich patches are still silica-rich when compared to stoichiometric minerals such as olivine or pyroxene (see Table 5). Several of these patches define the outlines of "ghost-mineral or mineral assemblages" that were present in the precursor cometary particles. The patches are never larger than one micrometer and are frequently separated by several microns from each other. These observations are consistent with the proposed loosely aggregated morphology of Wild 2 dust (Zolensky et al. 2006; Hörz et al. 2006; Brownlee et al. 2006) that were disaggregated and were dispersed on fine scales into molten aerogel.

The composition gradients between the dust-rich patches and silica-rich matrix are very sharp (Figs. 13–16). Mixing with aerogel was incomplete. As the heating event duration was very short and localized, the melted particles or fragments can be in close proximity with unmelted aerogel, showing that the temperature gradients were very steep at a submicron scale. These observations suggest that the silicate melts have been quenched rapidly into glass, avoiding a full mixing between the melted dust components and melted aerogel. Mixing of the melted silicate dust from the comet with a silica melt is not a thermodynamically favorable condition. Indeed, most of the binary phase diagrams with SiO_2 display a liquid immiscibility

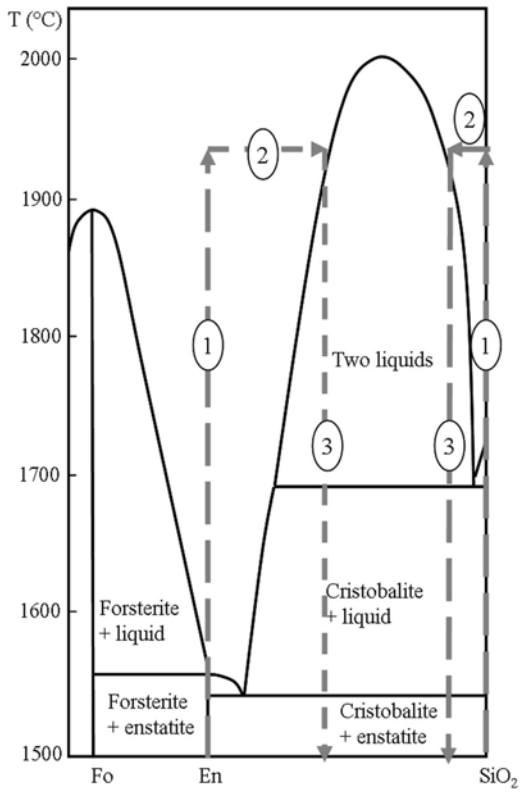

Fig. 18. Phase diagram of binary MgO-SiO_2 system for the region Mg_2SiO_4 (forsterite–Fo) SiO_2. The incoming minerals (here enstatite; En) and silica-aerogel are heated to high temperatures. The heating process is very abrupt, thus multicomponent melting such as congruent or incongruent melting does not occur (path 1). At high temperatures kinetics are very rapid and thus the melt products (enstatite and SiO_2 melts) will tend to equilibrate along path 2. Kinetically, the full equilibration may be stopped before accomplishment, but the enstatite melt tends to be enriched in SiO_2, and the SiO_2 melt (aerogel) tends to incorporate MgO. The liquids are then quenched along path 3. The silicate "dust-rich" patch compositions show a relatively high silica concentration and would be in good agreement with this scheme. The silicate melts are then relatively isolated from the aerogel melt. Their compositions are related to the precursor silicate components and allow attempting their recognition.

domain at high temperature (e.g., Mysen and Richet 2005 and references therein) that precludes mixing between almost pure SiO_2 melt and a melt having composition close to silicates such as olivine, pyroxenes, or other incoming oxides. Figure 18 shows a schematic representation of the MgO-SiO_2 phase. The diagram shows a high-silica liquid immiscibility field that closes at ~2000 °C. The temperature-composition paths for heating and quenching are indicated. Complete equilibrium is probably not fully reached, but the extended miscibility gap is a strong thermodynamic barrier, which precludes mixing between the two melts. This figure also explains why the silicate dust-rich areas are enriched in silica compared to the stoichiometry of silicate minerals. The composition of the quench product would give significant information about

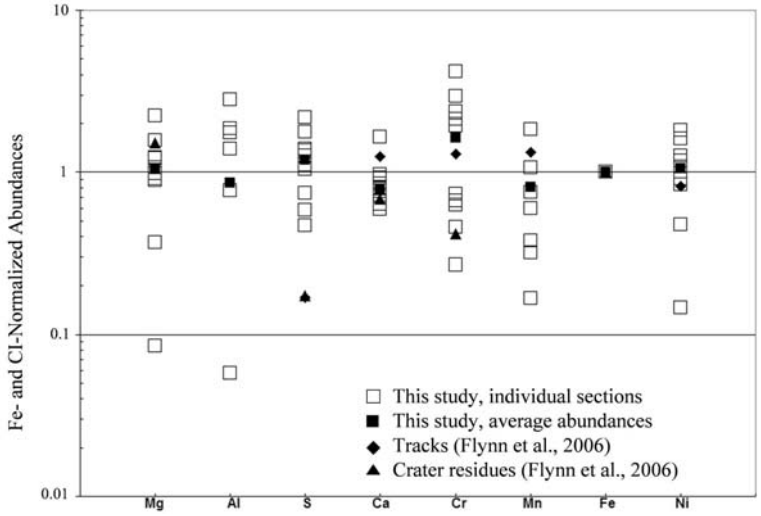

Fig. 19. Fe- and CI-normalized abundances of the bulk compositions for the allocations listed in Table 3 (open squares) and their calculated mean average abundances (solid squares) compared to the abundances for crater residues (solid triangles) and tracks (solid diamonds) taken from Flynn et al. (2006).

the thermal history. The presence of these dust-rich patches indicates that the melting temperature did not exceed the top of the miscibility gap at ~2000 °C. A comparable situation is encountered in magmas for which immiscibility of "olivine-basaltic" and rhyolitic magmas is observed (e.g., Roedder and Weiblen 1970). Shock-induced melts were also demonstrated to preserve high-silica glasses from mixing with other glass compositions. The low-pressure silica glass, named lechatelierite, often mixes incompletely with the other melt before cooling, leading to flow structure (schlieren) when the melt is subjected to shear deformation (e.g., See et al. 1998). Schaal (1982) demonstrated experimentally that shock-melting mixtures of silica glass and olivine powder does not induce full mixing of both melt products. Kinetic factors probably played a role, particularly during quenching of silicate melts, and perhaps even vapors, that would cause the formation of intermediate, deep metastable eutectic solid compositions that are both well-defined and different from stoichiometric silicate mineral compositions (Nuth et al. 2002; Rietmeijer 1999, 2002). Such non-stoichiometric solids will always be amorphous (Rietmeijer et al. 1999).

Toward a Reconstruction of the Original Particle Mineralogy

Wild 2 silicate mineral survivors are rare in our samples. They are all relatively large (several hundred nm) and developed amorphous partial rims that indicate partial melting. Wild 2 silicate signatures mainly occur as small-sized amorphous Mg-rich "dust-rich" patches with individual ghost crystals or assemblages that are quench products of fully melted silicate grains or sub-grains. They are mostly smaller than the TEM foil thickness (typically 80–100 nm). This configuration precludes analyzing them without including silica-rich glass. For some large dust-rich patches, for which overlap with the silica-rich glassy matrix apparently has not occurred, we have found Si/Mg ratios higher than unity (Table 5). This trend is in good agreement with the formation mechanism presented on Fig. 18, in which the silica enrichment can be explained by an equilibration of the two immiscible melts (silica-rich and Mg-rich) during the high-temperature excursion along their miscibility lines.

Most of the "dust-rich" patches contain significant Mg as the major element, whereas other elements (e.g., Al, Ca, Cr, Mn) are absent or are present in minor quantities. They might correspond to olivine and/or pyroxene Wild 2 materials. In some cases, Mg-rich areas contain Ca in low concentration while others have no detectable Ca (Figs. 14 and 16). Since the Ca content in olivine or orthoenstatite is usually very low, the Ca-free areas could correspond to these precursor minerals. The areas containing Ca have a Ca/Mg ratio ranging from 0.02 to 0.1, and could correspond to a low-Ca pyroxene such as pigeonite. The Mg-rich patches in C2044,2,41,3,6 do not contain apparent Fe-Ni-S droplets, but we have detected noticeable sulfur. We do not know if S is present in the form of very small clusters of iron-sulfides or as free S interstitial atoms trapped in the glass. Still, we calculated an MgO/(MgO + FeO) ratio of ~94% by assuming all Fe is present in the silicate. This value is increased to 97% if we assume that very small FeS phases or molecules are present. We have found two dust-rich patches that could correspond to an aluminum oxide (see Fig. 14) and a Ca-rich pyroxene (Ca/Mg ~ 1). If the Al-rich patch originated from corundum, this indicates that the melting temperature was very high in this particular aerogel volume indicating heterogeneous thermal spikes during impact collection.

The dust rich-materials are found as isolated submicron-sized patches dispersed within silica-rich melted aerogel, i.e., the glassy matrix with the opaque inclusions. This configuration is in good agreement with disaggregation

of the fine-grained portion of loosely aggregated Wild 2 dust in the model first discussed by Zolensky et al. (2006), Hörz et al. (2006), and Flynn et al. (2006). The mineralogy we tentatively reconstructed suggests that our samples were dominated by incoming submicron olivine and pyroxene grains with high MgO/(MgO + FeO) ratios, in agreement with the dominant Wild 2 olivine and pyroxene minerals (Zolensky et al. 2006).

Wild 2 Dust Compositions: Chondritic or Not?

Based on 23 whole-track and seven impact crater residues, Flynn et al. (2006) have determined that the bulk composition for the major rock-forming elements in comet Wild 2 dust is consistent with the CI composition within 35%, but with a larger deviation (within 60% of CI) for Ca and Ti. The sulfur abundance is well below the CI value. Flynn et al. (2006) also reported a high degree of chemical variability among individual tracks and the possibility that the size of impacting Wild 2 dust particles and the variations in the grain size distributions among their constituents could be cause of chemical heterogeneity. Despite complete melting and mixing of the comet dust with aerogel, the mixing lines in Fig. 5 based on EDS analyses show that the admixture of Wild 2 materials with the silica matrix was typically 10% assuming a CI (Anders and Ebihara 1982) bulk composition for this comet's dust. Our average, Fe- and CI-normalized compositions obtained from several TEM sections (Fig. 19, constructed from Table 3), which can be treated as small-volume bulk analyses of the silica-rich matrix, show element variations similar to those reported by Flynn et al. (2006), but with higher abundances for sulfur. The calculated mean values for our data are perfectly CI for some but closer to CI than the whole-track and crater residue data from Flynn et al. (2006). Sulfur is almost perfectly CI, which confirms that some S is finely distributed in compacted or melted aerogel, as suggested by Flynn et al. (2006). Sulfur is found as S-rich rims on opaque inclusions and rare "sulfur hot spots." Time-of-flight secondary ion mass spectrometry (ToF-SIMS) data for cometary material in C2115,30,21,0 and C2115,34,21,0 show close to Fe- and CI-normalized abundances—for Mg, Al, Cr, and Mn close to the CI abundances, Ca is much lower than CI, and above CI Ni abundances (Stephan et al. 2008). The high Ni abundances are within the range shown in Fig. 19 for this element, but Ca is much lower than the range reported here.

Bulk compositions of Wild 2 particles caught in aerogel were mostly measured by synchrotron X-ray fluorescence (SXRF), but this technique does not precisely measure elements such as Mg and Al. Our study shows that EDS analysis is a highly complementary technique tool for light elements such as Mg, Al, and S.

The mostly chondritic chemical compositions, except slightly higher Cr abundances, for the thermally modified samples (Fig. 19) suggest they originated from fine-grained comet materials rather than micron-sized minerals such as found among terminal particles (cf. Zolensky et al. 2006). Such fine-grained materials might resemble many aggregate IDPs or matrix in primitive chondrites. The Wild 2 dust-capture process better preserves coarse-grained or mono-mineralic particles rather than the fine-grained materials of the loosely bonded Wild 2 dust aggregates.

CONCLUSIONS

We presented the petrological properties of comet Wild 2 dust after its thermal interactions with the aerogel capture medium during hypervelocity impact. We identified aerogel that became densified during the capture process. The TEM slices we studied are characterized by a silica-rich matrix with numerous fine-grained (<100 nm) Fe-Ni-S inclusions that are randomly scattered. The inclusions have a distinct core-mantle structure but have variable core-rim ratios. The cores are Fe,Ni metal and low-S Fe-Ni-S phases; the rims are Fe sulfide (pyrrhotite), and rare high-S Fe-Ni-S phases that mostly define a mixing line between FeS and Ni-metal of low Ni content. High-Ni metal inclusions are present but rare. The silica-rich matrix can be highly vesicular, but vesicle number and sizes are highly heterogeneous. This matrix typically contains low amounts of Mg, Al, S, Ca, Cr, Mn, Fe, and Ni and traces of K. The matrix is host to highly vesicular, pure silica domains and common amorphous, dust-rich patches with much higher abundances of Mg, Al, Ca, and Fe. They are linked to surviving mineral grains, such as forsterite, Fe-rich forsterite, and pyroxene (pigeonite) that were present in our TEM sections, and refractory minerals, not seen in our sections.

The observations support melting of incident Wild 2 debris. The quench products define simple mixing lines between pure silica and comet sulfides and silicates in ratios of 5 to 15% chondritic comet dust to silica matrix. The Fe- and CI-normalized bulk compositions obtained by EDS analyses show that the fraction of Wild dust that was deposited in the capture cell material itself has a CI chondritic composition, including sulfur.

Our type of study based on allocated TEM sections has its inevitable drawback compared to "bulk-sample analyses." That is, our approach may lack important "three-dimensional data." It calls for a continuously updated database that tracks the histories of individual allocations and we are pleased to know that this effort is already underway at the curatorial level. Obviously, much more research needs to be done on Wild 2 particles, but TEM studies such as this will be very important for revealing the fine-grained component that forms the matrix of loosely bound Wild 2 aggregates and that appears to be uniquely deposited inside the capture cell material itself, in contrast to the larger constituents, which are found along track walls and at the track terminus.

Acknowledgments–The authors thank Keiko Nakamura-Messenger for the preparation of the ultramicrotomed TEM samples and helpful information about the preparation process. H. L., D. L., and P. C thank for the support from the electron microscope facility by European FEDER and region Nord-Pas-de-Calais. H. L., P. C., D. J., and M. G. thank the CNES (Centre National des Etudes Spatiales) for financial support. They thank Jean-François Dhenin for his assistance with the microscopes. M. G. thanks the France-USA program of the CNRS. F. J. M. R. was supported by grant NNG05GM84G from the NASA Headquarters Stardust Participating Scientist program (Stardust) for HRTEM analyses conducted in the Electron Microbeam Analyses Facility housed in the Department of Earth and Planetary Sciences (UNM) and by a grant from the NASA Goddard Space Flight Center. A. J. B. was supported by the NASA grant NNG06GG30G. F. L. acknowledges access to the TEM facilities at the Bayerisches Geoinstitut (Bayreuth) and financial support by the Deutsche Forschungsgemeinschaft. M. V. thanks Xudong Fan of MSU's CAM for assistance with TEM/EDS/SAED analyses; Rui Huang of MSU's Crystallography Service (Chemistry Department) for assistance with retrieval of diffraction data from JCPDS files; and Stanley Flegler (Director, MSU CAM) for supporting the TEM beam time. J. C. B. thanks Maureen MacKenzie in the Department of Physics and Astronomy at Glasgow for TEM assistance. R. M. S. and T. J. Z. acknowledge support from the Office of Naval Research and the NASA Stardust PE program. The authors thank an anonymous reviewer for a detailed review and constructive comments on the manuscript.

Editorial Handling—Dr. Donald Brownlee

REFERENCES

Anders E. and Ebihara M. 1982. Solar-system abundances of the elements. *Geochimica et Cosmochimica Acta* 46:2363–2380.

Anderson W. and Ahrens T. J. 1994. Physics of interplanetary dust capture via impact into organic foam. *Journal of Geophysical Research* E99:2063–2071.

Anderson W. 1998. Physics of interplanetary dust collection with aerogel. NASA/CR Technical Report 1998-207766.

Barrett R. A., Zolensky M. E., Hörz F., Lindstrom D., and Gibson E. K. 1992. Suitability of SiO_2 aerogel as a capture medium for interplanetary dust. Proceedings, 22nd Lunar and Planetary Science Conference. pp. 203–212.

Bennet M. E. and McSween H. Y. Jr. 1996. Shock features in iron-nickel metal and troilite of L-group ordinary chondrites. *Meteoritics & Planetary Science* 31:255–264.

Brownlee D., Tsou P., Aléon J., Alexander C. M. O'D., Araki T., Bajt S., Baratta G. A., Bastien R., Bland P., Bleuet P., Borg J., Bradley J. P., Brearley A., Brenker F., Brennan S., Bridges J. C., Browning N. D., Brucato J. R., Bullock E., Burchell M. J., Busemann H., Butterworth A., Chaussidon M., Cheuvront A., Chi M., Cintala M. J., Clark B. C., Clemett S. J., Cody G., Colangeli L., Cooper G., Cordier P., Daghlian C., Dai Z., D'Hendecourt L., Djouadi Z., Dominguez G., Duxbury T., Dworkin J. P., Ebel D. S., Economou T. E., Fakra S., Fairey S. A. J., Fallon S., Ferrini G., Ferroir T., Fleckenstein H., Floss C., Flynn G., Franchi I. A., Fries M., Gainsforth Z., Gallien J.-P., Genge M., Gilles M. K., Gillet Ph., Gilmour J., Glavin D. P., Gounelle M., Grady M. M., Graham G. A., Grant P. G., Green S. F., Grossemy F., Grossman L., Grossman J. N., Guan Y., Hagiya K., Harvey R., Heck P., Herzog G. F., Hoppe P., Hörz F., Huth J., Hutcheon I. D., Ignatyev K., Ishii H., Ito M., Jacob D., Jacobsen C., Jacobsen S., Jones S., Joswiak D., Jurewicz A., Kearsley A. T., Keller L. P., Khodja H., Kilcoyne A. L. D., Kissel J., Krot A., Langenhorst F., Lanzirotti A., Le L., Leshin L. A., Leitner J., Lemelle L., Leroux H., Liu M.-C., Luening K., Lyon I., MacPherson G., Marcus M. A., Marhas K., Marty B., Matrajt G., McKeegan K., Meibom A., Mennella V., Messenger K., Messenger S., Mikouchi T., Mostefaoui S., Nakamura T., Nakano T., Newville M., Nittler L. R., Ohnishi I., Ohsumi K., Okudaira K., Papanastassiou D. A., Palma R., Palumbo M. E., Pepin R. O., Perkins D., Perronnet M., Pianetta P., Rao W., Rietmeijer F. J. M., Robert F., Rost D., Rotundi A., Ryan R., Sandford S. A., Schwandt C. S., See T. H., Schlutter D., Sheffield-Parker J., Simionovici A., Simon S., Sitnitsky I., Snead C. J., Spencer M. K., Stadermann F. J., Steele A., Stephan T., Stroud R., Susini J., Sutton S. R., Suzuki Y., Taheri M., Taylor S., Teslich N., Tomeoka K., Tomioka N., Toppani A., Trigo-Rodríguez J. M., Troadec D., Tsuchiyama A., Tuzzolino A. J., Tyliszczak T., Uesugi K., Velbel M., Vellenga J., Vicenzi E., Vincze L., Warren J., Weber I., Weisberg M., Westphal A. J., Wirick S., Wooden D., Wopenka B., Wozniakiewicz P., Wright I., Yabuta H., Yano H., Young E. D., Zare R. N., Zega T., Ziegler K., Zimmermann L., Zinner E., and Zolensky M. 2006. Comet 81P/Wild 2 under a microscope. *Science* 314: 1711–1716.

Burchell M. J., Thomson R., and Yano H. 1999. Capture of hypervelocity particles in aerogel: In ground laboratory and low Earth orbit. *Planetary and Space Science* 47:189–204.

Burchell M. J., Graham G., and Kearsley A. 2006a. Cosmic dust collection in aerogel. *Annual Review of Earth and Planetary Sciences* 34:385–418.

Burchell M. J., Mann J., Creighton J. A., Kearsley A. T., Graham G., and Franchi I. A. 2006b. Identification of minerals and meteoritic materials via Raman techniques after capture in hypervelocity impacts on aerogel. *Meteoritics & Planetary Science* 41: 217–232.

Cliff R. A. and Lorimer G. W. 1975. The quantitative analysis of thin specimens. *Journal of Microscopy* 103:203–207.

Dominguez G., Westphal A. J., Phillips M. L. F., and Jones S. M. 2003. A fluorescent aerogel for capture and identification of interplanetary and interstellar dust. *The Astrophysical Journal* 592:631–635.

Domínguez G., Westphal A. J., Jones S. M., and Phillips M. L. F. 2004. Energy loss and impact cratering in aerogels: Theory and experiment. *Icarus* 172:613–624.

Flynn G. J., Bleuet P., Borg J., Bradley J. P., Brenker F. E., Brennan S., Bridges J., Brownlee D. E., Bullock E. S., Burghammer M., Clark B. C., Dai Z. R., Daghlian C. P., Djouadi Z., Fakra S., Ferroir T., Floss C., Franchi I. A., Gainsforth Z., Gallien J.-P., Gillet Ph., Grant P. G., Graham G. A., Green S. F., Grossemy F., Heck P. R., Herzog G. F., Hoppe P., Hörz F., Huth J., Ignatyev K., Ishii H. A., Janssens K., Joswiak D., Kearsley A. T., Khodja H., Lanzirotti A., Leitner J., Lemelle L., Leroux H., Luening K., MacPherson G. J., Marhas K. K., Marcus M. A., Matrajt G., Nakamura T., Nakamura-Messenger K., Nakano T.,

Newville M., Papanastassiou D. A., Pianetta P., Rao W., Riekel C., Rietmeijer F. J. M., Rost D., Schwandt C. S., See T. H., Sheffield-Parker J., Simionovici A., Sitnitsky I., Snead C. J., Stadermann F. J., Stephan T., Stroud R. M., Susini J., Suzuki Y., Sutton S. R., Taylor S., Teslich N., Troadec D., Tsou P., Tsuchiyama A., Uesugi K., Vekemans B., Vicenzi E. P., Vincze L., Westphal A. J., Wozniakiewicz P., Zinner E., and Zolensky M. E. 2006. Elemental compositions of comet 81P/Wild 2 samples collected by Stardust. *Science* 314:1731–1735.

Hsieh K. C., Chang Y. A., and Zhong T. 1982. The Fe-Ni-S system above 700 °C (iron-nickel-sulfur). *Bulletin of Alloy Phase Diagrams* 3:165–172.

Hsieh K. C., Vlach K. C., and Chang Y. A., 1987. The Fe-Ni-S system—I. A thermodynamic analysis of the phase equilibria and calculation of the phase diagram from 1173–1623 K. *High-Temperature Science* 23:17–38.

Hörz F., Cintala M. J., Zolensky M. E., Bernhard R. B., Davidson W. E., Haynes G., See T. H., Tsou P., and Brownlee D. E. 1998. Capture of hypervelocity particles with low density aerogel. NASA/TM Technical Report 98-201792.

Hörz F., Zolensky M. E., Bernhard R. P., See T. H., and Warren J. L. 2000. Impact features and projectile residues in aerogel exposed on Mir. *Icarus* 147:559–579.

Hörz F., Bastien R., Borg J., Bradley J. P., Bridges J. C., Brownlee D. E., Burchell M. J., Chi M., Cintala M. J., Dai Z. R., Djouadi Z., Dominguez G., Economou T. E., Fairey S. A. J., Floss C., Franchi I. A., Graham G. A., Green S. F., Heck P., Hoppe P., Huth J., Ishii H., Kearsley A. T., Kissel J., Leitner J., Leroux H., Marhas K., Messenger K., Schwandt C. S., See T. H., Snead C., Stadermann F. J., Stephan T., Stroud R., Teslich N., Trigo-Rodríguez J. M., Tuzzolino A. J., Troadec D., Tsou P., Warren J., Westphal A., Wozniakiewicz P., Wright I., and Zinner E. 2006. Impact features on Stardust: Implications for comet 81P/Wild 2 dust. *Science* 314:1716–1719.

Jarosewich E. 1990. Chemical analyses of meteorites: A compilation of stony and iron meteorite analyses. *Meteoritics* 25:323–337.

Kearsley A. T., Graham G. A., McDonnell J. A. M., Taylor E. A., Drolshagen G., Chater R. J., McPhail D., and Burchell M. J. 2007. The chemical composition of micrometeoroids impacting upon the solar arrays of the Hubble Space Telescope. *Advances in Space Research* 39:590–604.

Kullerud G., Yund R. A., and Moh G. H. 1969. Phase relations in the Cu-Fe-S, Cu-Ni-S, and Fe-Ni-S systems. Economic Geology Monograph 4. pp. 323–343.

Leroux H., Doukhan J. C., and Guyot F. 2000. Metal/silicate interaction in quenched shock-induced melt of the Tenham L6 chondrite. *Earth and Planetary Science Letters* 179:477–487.

Matrajt G. and Brownlee D. E. 2006. Acrylic embedding of Stardust particles encased in aerogel. *Meteoritics & Planetary Science* 41:1715–1720.

Nuth J. A. III, Rietmeijer F. J. M., and Hill H. G. M. 2002. Condensation processes in astrophysical environments: The composition and structure of cometary grains. *Meteoritics & Planetary Science* 37:1579–1590.

Mysen B. O. and Richet P. 2005. Silicate glasses and melts: Properties and structure. In *Developments in geochemistry,* vol. 10. Amsterdam: Elsevier. pp. 169–198.

Noguchi T., Nakamura T., Okudaira K., Yano H., Sugita S., and Burchell M. J. 2007. Thermal alteration of hydrated minerals during hypervelocity capture to silica aerogel at the flyby speed of Stardust. *Meteoritics & Planetary Science* 42:357–372.

Okudaira K., Noguchi T., Nakamura T., Sugita S., Sekine Y., and Yano H. 2004. Evaluation of mineralogical alteration of micrometeoroid analog materials captured in aerogel. *Advances in Space Research* 34:2299–2304.

Perin L., Calas-Etienne S., Faivre A., and Phalippou J. 2003. Sintering of compressed aerogels. *Journal of Non-Crystalline Solids* 325:224–229.

Phalippou J., Despetis F., Calas S., Faivre A., Dieudonné P., Sempéré R., and Woignier T. 2004. Comparison between sintered and compressed aerogels. *Optical Materials* 26:167–172.

Rietmeijer F. J. M. 1998. Interplanetary dust particles. In *Planetary materials*, edited by J. J. Papike. Reviews in Mineralogy, vol. 36. Chantilly, Virginia: Mineralogical Society of America. pp. 2-1–2-95.

Rietmeijer F. J. M. 1999. Metastable non-stoichiometric diopside and Mg-wollastonite: An occurrence in an interplanetary dust particle. *American Mineralogist* 84:1883–1894

Rietmeijer F. J. M. 2002. The earliest chemical dust evolution in the solar nebula. *Chemie der Erde* 62:1–45.

Rietmeijer F. J. M. 2004. Dynamic pyrometamorphism during atmospheric entry of large (~10 micron) pyrrhotite fragments from cluster IDPs. *Meteoritics & Planetary Science* 39:1869–1887.

Rietmeijer F. J. M., Nuth J. A. III, and Karner J. M. 1999. Metastable eutectic condensation in a Mg-Fe-SiO-H_2-O_2 vapor: Analogs to circumstellar dust. *The Astrophysical Journal* 527:395–404.

Rietmeijer F. J. M., Nakamura T., Tsuchiyama A., Uesugi K., Nakano T., and Leroux H. 2008. Origin and formation of iron-silicide phases in the aerogel of the Stardust mission. *Meteoritics & Planetary Science* 43. This issue.

Roedder E. and Weiblen P. A. 1970. Silicate immiscibility in lunar magmas, evidenced by melt inclusions in lunar rocks. *Science* 167:641–644.

Schaal R. B. 1982. Disequilibrium features in experimentally shocked mixtures of olivine plus silica glass powders. *Contributions to Mineralogy and Petrology* 81:39–47.

Scherer G. W., Calas S., and Sempéré R. 1998. Densification kinetics and structural evolution during sintering of silica aerogel. *Journal of Non-Crystalline Solids* 240:118–130.

See T. H., Wagstaff J., Yang V., Hörz F., and McKay G. A. 1998. Compositional variation and mixing of impact melts on microscopic scales. *Meteoritics & Planetary Science* 33:937–948.

Shi F., Wang L., and Liu J. 2006. Synthesis and characterization of silica aerogels by a novel fast ambient pressure drying process. *Materials Letters* 60:3718–3722.

Stephan T., Rost D., Vicenzi E. P., Bullock E. S., MacPherson G. J., Westphal A. J., Snead C. J., Flynn G. J., Sandford S. A., and Zolensky M. E. 2008. TOF-SIMS analysis of cometary matter in Stardust aerogel tracks. *Meteoritics & Planetary Science* 43. This issue.

Sugaki A. and Kitakaze A. 1998. High form of pentlandite and its thermal stability. *American Mineralogist* 83:133–140.

Stroud R. M., Long J. W., Pietron J. J., and Rolison D. R. 2004. A practical guide to transmission electron microscopy of aerogels. *Journal of Non-Crystalline Solids* 350:277–284.

Trucano T. G. and Grady D. E. 1995. Impact shock and penetration fragmentation in porous media. *International Journal of Impact Engineering* 17:861–872.

Tsou P. 1995. Silica aerogel captures cosmic dust intact. *Journal of Non-Crystalline Solids* 186:415–427.

Van Cappellen E. 1990. The parameterless correction method in X-ray microanalysis. *Microscopy Microanalysis Microstructure* 1:1–22.

Van Cappellen E. and Doukhan J. C. 1994. Quantitative transmission X-ray microanalysis of ionic compounds. *Ultramicroscopy* 53:343–349.

Westphal A. J., Snead C., Borg J., Quirico E., Raynal P. I., Zolensky M. E., Ferrini G., Colangeli L., and Palumbo P. 2002. Small hypervelocity particles captured in aerogel collectors: Location, extraction, handling, and storage. *Meteoritics & Planetary Science* 37:855–865.

Zolensky M. E., Zega T. J., Yano H., Wirick S., Westphal A. J., Weisberg M. K., Weber I., Warren J. L., Velbel M. A., Tsuchiyama A., Tsou P., Toppani A., Tomioka N., Tomeoka K., Teslich N., Taheri M., Susini J., Stroud R., Stephan T., Stadermann F. J., Snead C. J., Simon S. B., Simionovici A., See T. H., Robert F., Rietmeijer F. J. M., Rao W., Perronnet M. C., Papanastassiou D. A., Okudaira K., Ohsumi K., Ohnishi I., Nakamura-Messenger K., Nakamura T., Mostefaoui S., Mikouchi T., Meibom A., Matrajt G., Marcus M. A., Leroux H., Lemelle L., Le L., Lanzirotti A., Langenhorst F., Krot A. N., Keller L. P., Kearsley A. T., Joswiak D., Jacob D., Ishii H., Harvey R., Hagiya K., Grossman L., Grossman J. N., Graham G. A., Gounelle M., Gillet Ph., Genge M. J., Flynn G., Ferroir T., Fallon S., Ebel D. S., Dai Z. R., Cordier P., Clark B., Chi M., Butterworth A. L., Brownlee D. E., Bridges J. C., Brennan S., Brearley A., Bradley J. P., Bleuet P., Bland P. A., and Bastien R. 2006. Mineralogy and petrology of comet 81P/Wild 2 nucleus samples. *Science* 314:1735–1739.